Review article

Michael Chen, Minseok Kim, Alex M.H. Wong and George V. Eleftheriades*

Huygens' metasurfaces from microwaves to optics: a review

Abstract: In this article, the basic principles and the main applications of Huygens' metasurfaces (HMSs) are reviewed from microwaves to optics. In general, HMSs comprise a thin layer of orthogonal electric and magnetic dipoles, which form an array of Huygens' sources. In a refraction setting, these sources radiate mostly in the forward direction and can be used to manipulate an incident electromagnetic wave at will. In the case of passive HMSs, the Huygens' sources are induced by an incident electromagnetic field. Examples of passive manipulations include reflectionless refraction, perfect anomalous reflection, and arbitrary antenna beam forming. In the case of active HMSs, the Huygens' sources are impressed active sources. Active HMS manipulations include cloaking and subwavelength spot formation in a cavity environment.

Keywords: metasurfaces; Huygens' principle; wavefront manipulation; perfect refraction; perfect anomalous reflection; cloaking; antenna beam forming.

1 Introduction/History

The shaping of electromagnetic waves by dielectric lenses and metallic reflectors such as parabolic mirrors is a well-established discipline in optics and microwave antenna engineering [1–4]. However, both dielectric lenses and reflectors lead to considerable volume and weight, especially at microwave and even millimeter-wave frequencies. For these reasons, in the past decades, there has been considerable research to make flat versions of these fundamental wave-shaping devices. At microwaves, there is the well-established field of transmitarrays (to replace lenses) and reflectarrays (to replace reflectors) [5–9]. Likewise, mostly in the optical regime, planar gratings and holographic surfaces based on diffraction effects have been developed for various applications [10–16]. Transmit and reflectarrays typically comprise arrays of elementary antennas (e.g. dipoles or patches) printed on a flat dielectric substrate. The required phasing to achieve a certain wavefront transformation (e.g. to focus an incident plane wave) is provided by spatially modulating the size or the shape of these elementary antennas. Typically, this is accomplished by working close to the resonance of these elementary antennas to obtain the required phase range. Hence, these constituent antenna elements are usually half wavelength in size. Moreover, in the case of transmitarrays, several layers are needed to achieve good matching characteristics and avoid reflections. While traditionally, transmitarrays have been confined to the microwave regime, optical transmitarrays have been reported in recent years due to the advent of precise nanofabrication techniques. Prominent examples on this front include the pioneering work reported in Ref. [17, 18]. On the other hand, diffraction gratings and holographic surfaces have been traditionally more popular in the optical regime (due to their size, which needs to be several wavelengths long). Primarily, these are periodic structures that manipulate fields in a scalar fashion. Because conventional gratings have unit-cell dimensions comparable to the wavelength, these are diffractive structures. In recent years, gratings and related holographic structures have also been developed for antenna applications at microwaves. In fact, such structures can now handle full tensor-field transformations and hence can manipulate polarization as well [19, 20].

In this review article, we report recent advances in Huygens' metasurfaces (HMSs), which are engineered surfaces also designed for the manipulation of incident electromagnetic waves. These surfaces are related to transmit- and reflectarrays but with some key differences [21–23]. Some of these include the fact that these HMSs are

*Corresponding author: George V. Eleftheriades,** The Edward S. Rogers Department of Electrical and Computer Engineering, University of Toronto, Toronto, Ontario, M5S 3G4 Canada, e-mail: gelefth@waves.utoronto.ca
Michael Chen, Minseok Kim and Alex M.H. Wong: The Edward S. Rogers Department of Electrical and Computer Engineering, University of Toronto, Toronto, Ontario, M5S 3G4 Canada

typically subwavelength thin and their constituent unit cells are also subwavelength. Because of the subwavelength scales involved, these surfaces can be homogenized and characterized by spatially varying surface impedances and admittances. This is what justifies the name "metasurface," which can be thought of as two dimensional (2D) "metamaterials" and also described in terms of electric and magnetic susceptibilities [24]. The conceptual realization of these metasurfaces is based on the Schelkunoff's equivalence principle, which is the generalization of Huygens' principle: a known incident electromagnetic wave is transformed to a desired one, resulting to field discontinuities that induce electric and magnetic currents on the metasurface (interface), as depicted in Figure 1 [22, 25]. These electric and magnetic currents are physically realized using co-located orthogonal electric and magnetic dipoles that correspond to spatially varying admittance and impedance sheet distributions [21, 22, 26]. It should be pointed out that these equivalent electric and magnetic currents can be made impressed instead of induced, which leads to the concept of active HMSs, which in fact preceded the passive ones [27, 28].

Because of the subwavelength nature of the constituent unit cells and the fact that both electric and magnetic currents are induced according to Maxwell's equations (rigorous boundary conditions), these HMSs have some interesting intrinsic features: they are naturally well matched even though they are subwavelength thin, and they do not excite spurious radiation modes (such as higher Floquet modes in the case of simple refraction) [29]. In principle, this approach can be used to deterministically design such engineered surfaces to manipulate all attributes of the incident field: its magnitude, phase, and
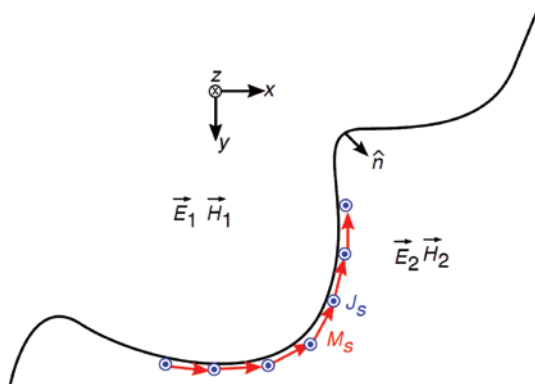
Figure 1: An incident electromagnetic field ($\vec{E}_1$, $\vec{H}_1$) is converted to a transmitted field ($\vec{E}_2$, $\vec{H}_2$) through a field discontinuity, sustained by induced orthogonal electric and magnetic currents ($\vec{J}_s$, $\vec{M}_s$) supported by an engineered electromagnetic surface (metasurface); obtained from Ref. [22].

polarization. Some notable successes of HMSs include subwavelength thin "perfect refracting" surfaces that suffer no reflections whatsoever and all incident power is coupled to the refracted beam. Likewise, "perfect reflecting" metasurfaces can be designed (akin to reflectarrays), which can transfer 100% of the incident power to an arbitrary reflection angle. Moreover, because of this total field control that can be enabled by such metasurfaces, aperture antennas can be designed with prescribed characteristics such as beamwidth, beam-pointing direction, and sidelobe-level distribution. Other applications such as absorbing metasurfaces can also be achieved [30–33]. In the remainder of this article, we elaborate on some of these HMS topics summarizing the basic principles involved and highlighting the latest developments.

2 Basic theory of HMSs

As previously mentioned, HMSs are thin electromagnetic devices that can perform desired field transformations, specifically through the utilization of the Schelkunoff's equivalence principle [21, 22, 25, 34]. As seen in Figure 1 and Eq. (1), when fields $\vec{E}_1$, $\vec{H}_1$, and $\vec{E}_2$, $\vec{H}_2$ are stipulated in two half spaces, the electric ($\vec{J}_s$) and magnetic ($\vec{M}_s$) current densities required to transform the fields from one domain to the other can be obtained [25, 35], where $\vec{E}_1^-$, $\vec{H}_1^-$, $\vec{E}_2^+$, and $\vec{H}_2^+$ are the respective values of $\vec{E}_1$, $\vec{H}_1$, $\vec{E}_2$, and $\vec{H}_2$ at the boundary of the field discontinuity.

$$\vec{J}_s = \hat{n} \times (\vec{H}_2^+ - \vec{H}_1^-), \quad \vec{M}_s = -\hat{n} \times (\vec{E}_2^+ - \vec{E}_1^-) \tag{1}$$

In this fashion, to produce an HMS, the desired structure simply needs to realize the necessary surface current densities for any given field transformation [21, 22]. As mentioned, one such approach of realizing these currents is to use impressed sources such as in Ref. [27, 28] and further elaborated in Section 3.5. In this method, the electric and magnetic current densities are directly introduced via external sources. The radiated fields of these impressed sources will then interact with the incident fields to produce the desired output fields. However, the utilization of impressed current sources is not always trivial. Some challenges include the generation and distribution of microwave/optical power, power consumption, and the precise realization of the required current weights [28]. Alternatively, these surface currents can be induced by the incident fields by synthesizing effective electric and magnetic properties. In this case, the metasurface is designed in terms of these intrinsic characteristics instead of arrays of impressed sources. By synthesizing these electric and

magnetic properties, the desired boundary surface current densities are excited by the incident fields, thus leading in principle to passive and lossless metasurfaces [36]. The scattered fields from these excited currents are then capable of producing the output fields by interacting with the incident wave. In general, there are three perspectives for designing these metasurface properties, which are the susceptibility [24, 37, 38], polarizability [36, 38–40], and impedance/admittance approaches [21, 22]. It should be noted that regardless of the chosen perspective, all these methods can achieve the same range of field manipulations [41]. In this review article, we will be mainly using the impedance/admittance perspective for demonstrative purposes. To introduce the electric and magnetic properties of the metasurface, the equivalence principle can be combined with another set of equations, which relate the average tangential fields at the desired boundary to the required current densities as seen in Eq. (2) [21, 22, 42].

$$\vec{E}_{t,\text{avg}} = \bar{\bar{Z}}_{se} \cdot \vec{J}_s, \quad \vec{H}_{t,\text{avg}} = \bar{\bar{Y}}_{sm} \cdot \vec{M}_s \tag{2}$$

In this case, the tensors $\bar{\bar{Z}}_{se}$ and $\bar{\bar{Y}}_{sm}$ represent the spatially varying electric impedance and magnetic admittance of the metasurface, respectively. Similarly to how an electric current density may be excited by an electric field due to the conductivity of the material, the electric impedance, $\bar{\bar{Z}}_{se}$, can be thought of in the same manner. Furthermore, a magnetic admittance can be introduced, which relates the magnetic current density to the tangential magnetic fields in the form of $\bar{\bar{Y}}_{sm}$ [21, 22]. In general, these impedance and admittance values are in the form of tensors, to account for any arbitrary polarization of the input and output fields [41, 43, 44]. However, in the case of single polarization surfaces, these tensor properties can be simplified to scalar quantities [41, 42]. By combining Eq. (1) and Eq. (2), a system of complex equations can be formed, which relates the field quantities at the interface of the field discontinuity to the electric impedance and magnetic admittance of the metasurface, as seen in Eq. (3) [42, 45].

$$\vec{E}_{t,\text{avg}} = \bar{\bar{Z}}_{se} \cdot [\hat{n} \times (\vec{H}_2^+ - \vec{H}_1^-)]$$
$$\vec{H}_{t,\text{avg}} = \bar{\bar{Y}}_{sm} \cdot [-\hat{n} \times (\vec{E}_2^+ - \vec{E}_1^-)] \tag{3}$$

By stipulating the desired incident fields $\vec{E}_1$ and $\vec{H}_1$ and the desired output fields $\vec{E}_2$ and $\vec{H}_2$, the electric impedance and magnetic admittance of the metasurface can then be obtained. Accurate modeling of these obtained impedance/admittance values can then be achieved by designing subwavelength unit cells as spatial sampling agents [24, 26, 46]. The overall metasurface, which is assembled using these unit cells, can then be physically realized.

In summary, HMSs are defined based on Figure 1 and Eq. (1), with the additional requirement that the surfaces can be homogenized using, for example, equivalent sheet impedances and/or admittances, as implied in Eq. (3). In this way, the excited electric and magnetic surface currents in Figure 1 can produce the desired fields according to Schelkunoff's equivalence principle, which is the generalization of the Huygens' principle [21, 25, 34, 47]. Specifically, the equivalent currents are $\vec{J}_s^+ = \hat{n} \times \vec{H}^+$, $\vec{M}_s^+ = -\hat{n} \times \vec{E}^+$ for region 2 and $\vec{J}_s^- = -\hat{n} \times \vec{H}^-$, $\vec{M}_s^- = \hat{n} \times \vec{E}^-$ for region 1, producing the reflected fields.

Applying similar derivations for designing HMSs as shown above, different wave transformations have been demonstrated, which include polarization control, wave refraction, and wave focusing [21–23, 43, 44, 48–53]. However, in certain applications, such as wide-angle refraction, it was found that the above derivations were unable to produce perfect or reflectionless transformations [22, 54]. Even in cases where no reflected fields were desired, the relations above were still not able to produce unity transformation of the desired input to the transmitted fields. These refraction surfaces often suffered from increased reflections as the refracted wave angles become more oblique relative to the incident wave angle [22, 29, 54]. This issue was studied in Ref. [42, 55–58], and the problem was identified to arise due to $\bar{\bar{Z}}_{se}$ and $\bar{\bar{Y}}_{sm}$ containing non-zero real components. For simplicity, we will restrict the discussion to the case of one-dimensional (1D) single polarization refraction surfaces for illustrative purposes. In this case, Eq. (3) and the tensor values $\bar{\bar{Z}}_{se}$ and $\bar{\bar{Y}}_{sm}$ will reduce to their scalar forms. Furthermore, Eq. (3) then forms a system of two complex equations with two complex unknowns, which leads to a unique solution. However, it was found that in these 1D single-polarization wide-angle refraction cases, the obtained complex impedance and admittance values contained both non-zero imaginary and real components [55–58]. Due to the requirement of $\bar{\bar{Z}}_{se}$ and $\bar{\bar{Y}}_{sm}$ values, which have non-zero real components, this resulted in the boundary conditions requiring control over loss and gain regions [55–58]. This meant that, without controlling these regions of the metasurface, these structures were unable to produce the desired perfect (i.e. reflectionless) refraction. This problem was first solved in Ref. [54] by treating the general refraction situation by means of generalized scattering matrices. This led to the proposal of using asymmetric metasurfaces such that matching can be achieved for the differing wave impedances of the incident and refracted waves. Subsequently, in Ref. [42, 55], it was shown that this approach corresponds to altering the original boundary conditions implied in (1) and (2).

This proposed method utilizes bianisotropy in the meta-surface, which allowed the coupling of its electric and magnetic responses [59]. This coupling introduced the possibility of excitation of both electric and magnetic current densities from both tangential electric and magnetic fields, in contrast to the above non-bianisotropic boundary conditions, which did not allow cross excitations to occur [42, 55, 60]. To introduce bianisotropy into the boundary conditions, the tensor magnetoelectric coupling coefficient $\bar{\bar{K}}_{em}$ could be introduced as seen in Eq. (4) and Eq. (5) [42].

$$\vec{E}_{t,\text{avg}} = \bar{\bar{Z}}_{se} \cdot \vec{J}_s - \bar{\bar{K}}_{em} \cdot [\hat{n} \times \vec{M}_s]$$
$$\vec{H}_{t,\text{avg}} = \bar{\bar{Y}}_{sm} \cdot \vec{M}_s - \bar{\bar{K}}_{em} \cdot [\hat{n} \times \vec{J}_s] \tag{4}$$

$$\vec{E}_{t,\text{avg}} = \bar{\bar{Z}}_{se} \cdot [\hat{n} \times (\vec{H}_2^+ - \vec{H}_1^-)] - \bar{\bar{K}}_{em} \cdot \{\hat{n} \times [-\hat{n} \times (\vec{E}_2^+ - \vec{E}_1^-)]\}$$
$$\vec{H}_{t,\text{avg}} = \bar{\bar{Y}}_{sm} \cdot [-\hat{n} \times (\vec{E}_2^+ - \vec{E}_1^-)] - \bar{\bar{K}}_{em} \cdot \{\hat{n} \times [\hat{n} \times (\vec{H}_2^+ - \vec{H}_1^-)]\} \tag{5}$$

In the new bianisotropic formulation, the introduction of the magnetoelectric coupling coefficient $\bar{\bar{K}}_{em}$ essentially allowed an extra degree of freedom to enable the choice of a lossless and passive solution [42, 61]. Utilizing this bianisotropy and applying local power conservation, the realization of a true lossless and passive solution for 1D single-polarization wide-angle refraction was finally achieved [42, 55, 60]. Although in this case, bianisotropy is discussed for the application of wave refraction, it can be used in any general case to introduce an additional degree of freedom for any complex field transformation [42, 55, 62–65].

3 HMS applications

3.1 HMS refraction

One of the earliest demonstrations of HMSs for low-reflection refraction was reported in Ref. [21, 26, 50]. Through theory, simulations, and experimental verifications, low-reflection refraction at microwave frequencies was observed [21, 50]. Examples of few of the fabricated refraction surfaces can be seen in Figure 2, displaying two examples of refracting surfaces with different design topologies. While in both cases, wire/loop unit cells were used to represent a Huygens' source, by realizing the electric response with metallic wires and the magnetic response with loops, the orientations of the two designs is quite different. In Ref. [21], the wire/loop unit cells were stacked in a transverse fashion, with the structures placed parallel to the direction of propagation. On the other hand, the unit cells in Ref. [50] were positioned in a single-plane configuration, with the unit cells perpendicular to the direction of propagation. Although physically orientated differently, both of these structures demonstrated good refractive properties and were able to successfully represent Huygens' sources. However, other designs have also been used to realize HMSs. One such structure is the multi-layer cascaded unit cell [42, 52, 54, 60]. Instead of an intuitive design afforded by the wire/loop unit cells presented in Ref. [21] and [50], the cascaded topology utilizes capacitive and inductive properties of stacked planar metallic patterns to obtain Huygens' unit cell performance. While these stacked planar structures do not contain physical
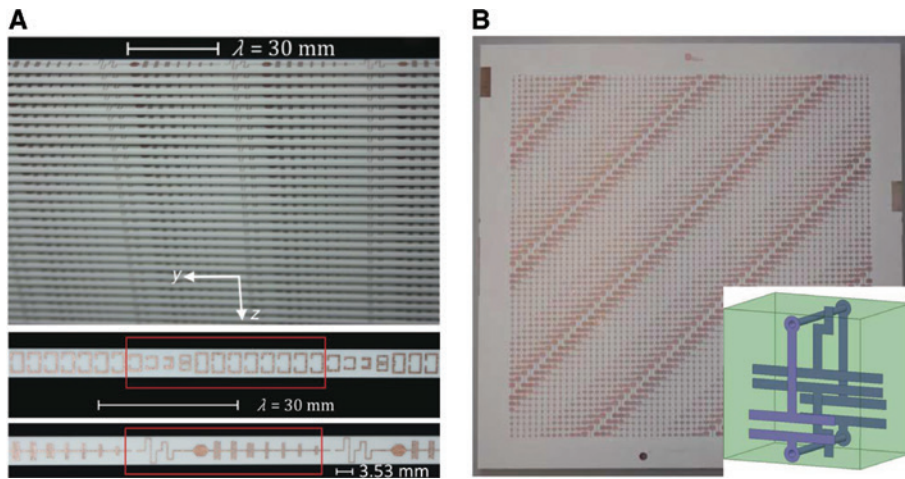
Figure 2: Samples of fabricated microwave refraction surfaces.
(A) Photograph of fabricated 1D refraction metasurface for 45° refraction of a normally incident TM plane wave at 10 GHz using transverse-stacked wire/loop unit cells. Obtained from Ref. (21). (B) Photograph of fabricated 2D refraction surface at 10 GHz using planar wire/loop unit cell structures lying on a single plane. Obtained from Ref. (50).

wires and loops to realize Huygens' sources, the cascaded effect of these capacitive and inductive geometries is still able to synthesize the required Z_{se} and Y_{sm} reactances that are needed by the boundary conditions in (3). Schematics of the two unit cell structures can be seen in Figure 3, and an example of a physical realization of the three-layer structure can be seen in Figure 9. Regardless of the difference in physical realization, all three topologies have demonstrated the capability of realizing Huygens' responses, specifically in the application of low-reflection refraction [21, 42, 50, 60].

It should be noted that even though the two unit cells in Figure 3 can generate the Z_{se} and Y_{sm} reactances that are required by Eq. (3), they are actually not equivalent. The wire/loop unit cell naturally synthesizes a Huygens' source, as it directly realizes the electric and magnetic currents stipulated by the equivalence principle. As was shown in Ref. [66], the equivalent circuit of the wire/loop unit cell is of the lattice topology, as shown in Figure 4A.

This arises from the fact that there is a one-to-one correspondence between the $\vec{E}$, $\vec{H}$ field boundary conditions across an interface and the corresponding V, I circuit terminal relations. One may assume that in the limit that the interlayer distance between the shunt admittances "d" diminishes, the three-shunt-admittance topology will converge to the wire/loop topology, but this is not the case. In fact, in such a case, the three-shunt admittance solution would diverge and can never achieve a lattice type of a response [54]. To appreciate this in a more dramatic way, one can exploit the lattice nature of the wire/loop approach and design a nearly allpass frequency response [67]. This is shown in Figure 4B where a very broad matching bandwidth can be achieved, thus opening up the possibility of broadband ultrathin HMSs, something that is not possible with the three-shunt-admittance unit cell. This effect can be further understood because the reflection coefficient from the loop (series branch in Figure 4A) is equal and opposite to the
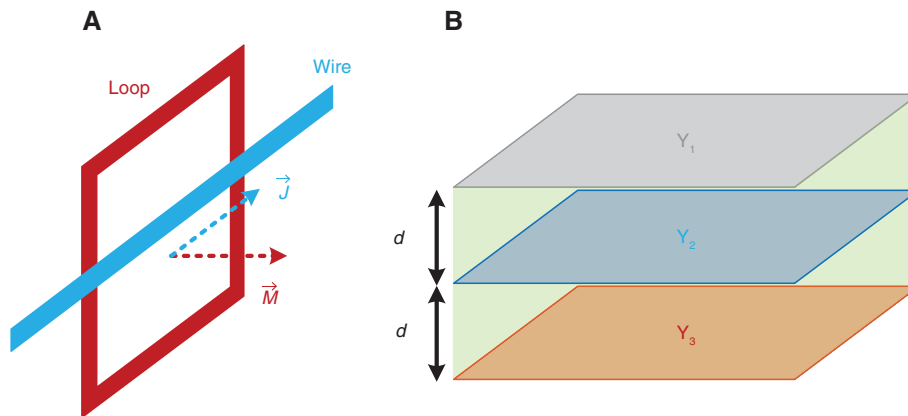
Figure 3: Two different realizations of Huygens' unit cells.
(A) Wire/loop unit cell. (B) Stacked three-layer shunt-admittance unit cell.
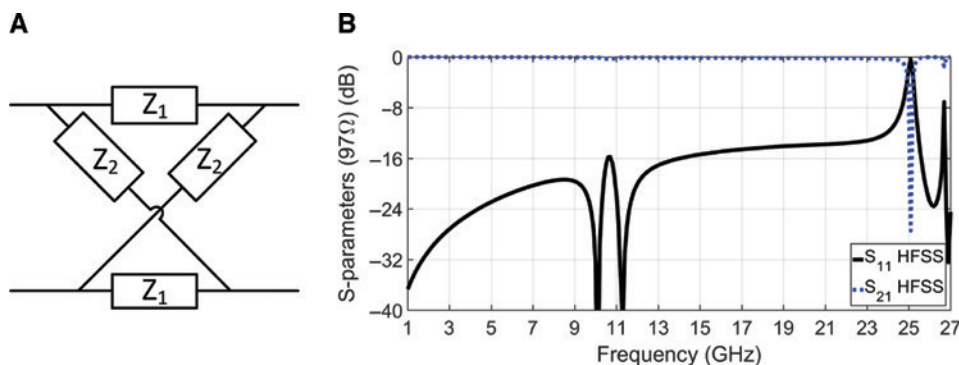
Figure 4: Lattice unit cell circuit model.
(A) Lattice circuit topology representing wire/loop unit cell. Obtained from Ref. [66]. (B) Ultra-broadband matched response of a wire/loop unit cell obtained from fullwave simulations. Obtained from [67].

reflection from the dipole (shunt branch in Figure 4A). An interesting related discussion based on the polarization inclusion approach, for absorber applications, can be found in Ref. [30].

As previously mentioned, it was shown in Ref. [22, 29, 41, 54–58] that the refraction efficiency of the first-generation refraction-surface designs deteriorated as the refraction angle became more oblique relative to the incident beam angle. Originally, these refraction surfaces were non-bianisotropic and thus were physically represented with symmetric structures [21–23, 29, 54, 55]. However, due to their physical symmetry, these metasurfaces were unable to simultaneously match both the incident and refracted wave impedances, which are angle-dependent [21–23, 29, 54, 55]. Therefore, as the desired refraction angle was increased, the impedance mismatch and the reflections correspondingly increased, which resulted in a reduction of the refraction efficiency, as shown in Figure 5 [41].

This issue fundamentally arose from the lack of degrees of freedom. As these surfaces were all designed to be passive devices, they were unable to produce the necessary gain and loss mechanisms required by the boundary conditions. To demonstrate this issue, we will examine a 1D wide-angle refraction of a normally incident transverse electric (TE) plane wave towards 71.8° at 20 GHz, as described in Ref. [42, 60]. Using the described desired TE refraction scenario, the obtained non-bianisotropic electric impedance and magnetic admittance can be seen in Figure 6.

As shown, for this wide-angle refraction, the obtained Z_{se} and Y_{sm} values contain non-zero real components, which translate to control over loss and gain regions [55–58]. Therefore, without realizing the required gain and
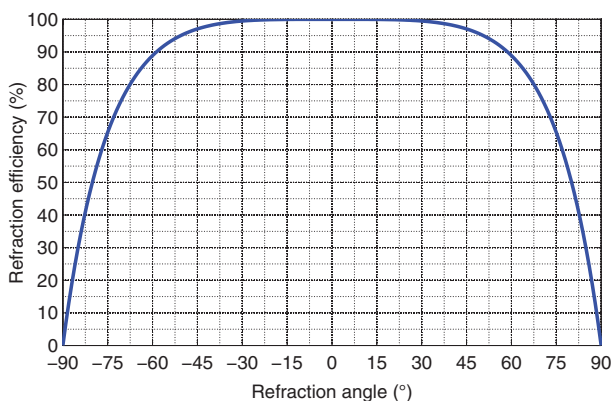
loss mechanisms, the refraction efficiency was reduced. As previously discussed, this is due to the lack of degrees of freedom to choose the desired lossless and passive solution. To introduce an extra degree of freedom, the use of bianisotropy can be included in the boundary condition formulations [42, 54, 55, 60]. Using the same refraction scenario with the bianisotropic boundary conditions and stipulating the lossless, passive, and local power conservation conditions [45], the corresponding Z_{se}, Y_{sm}, and K_{em} values can be seen in Figure 7.

Examination of the bianisotropic boundary conditions showed that the obtained Z_{se} and Y_{sm} values now are purely imaginary and K_{em} is purely real, which corresponds to a true lossless and passive design [42, 61]. In addition, translating these boundary conditions to generalized scattering or G parameters, as described in Ref. [42, 54, 60, 68, 69], results in perfect refraction with no reflection, as can be seen in Figure 8.

Using the bianisotropic boundary conditions, the demonstration of perfect or reflectionless refraction was theoretically demonstrated in Ref. [42, 55]. Later in Ref. [60], a physical realization of a printed circuit board (PCB) reflectionless refraction HMS was demonstrated. The fabricated prototype utilized a three-layer asymmetric structure, which exploited the physical asymmetry to synthesize the bianisotropy [54, 60]. A close-up of a section of the fabricated metasurface can be seen in Figure 9. The realized metasurface was able to achieve good refraction characteristics while causing minimal reflections for wide-angle refraction from normal incidence to 71.8° at 20 GHz [60]. The reflection and refraction of the metasurface were measured using a combination of quasi-optical (setup shown in Figure 10) and far-field measurements and can be seen in Figures 11 and 12.

Figure 5: Refraction efficiency as a function of the refraction angle with normally incident plane wave for a non-bianisotropic HMS. Obtained from Ref. [41].
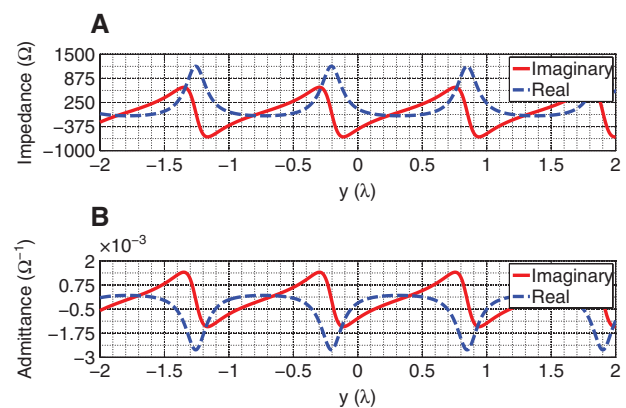
Figure 6: Non-bianisotropic boundary conditions for 0° to 71.8° TE refraction at 20 GHz.
(A) Imaginary and real components of Z_{se}. (B) Imaginary and real components of Y_{sm}.
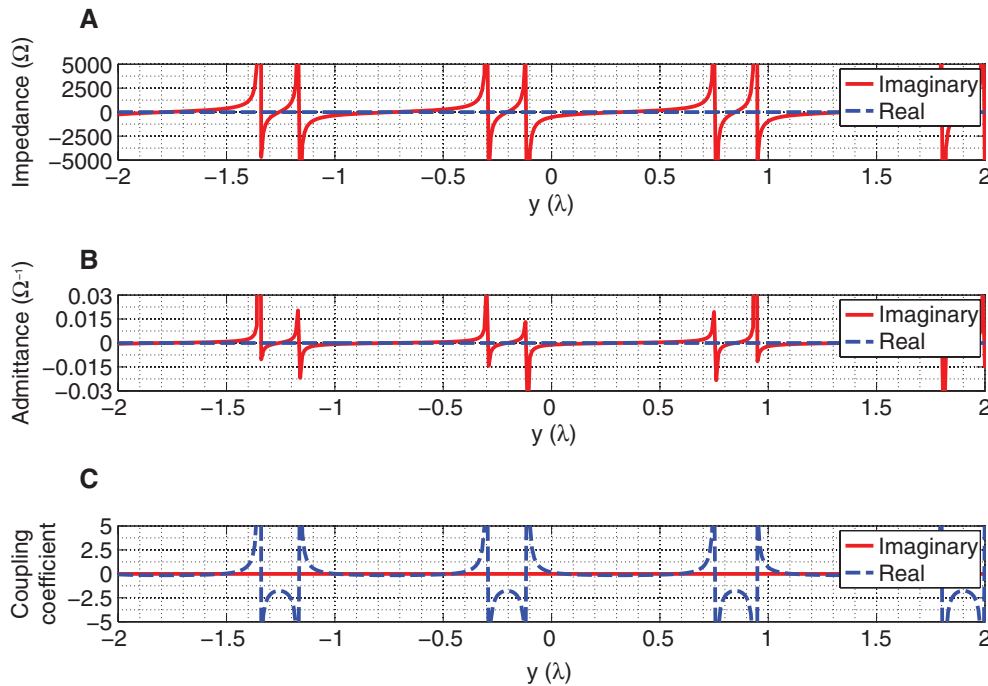
Figure 7: Bianisotropic boundary conditions for 0° to 71.8° TE refraction at 20 GHz.
(A) Imaginary and real components of Z_{se}. (B) Imaginary and real components of Y_{sm}. (C) Imaginary and real components of K_{em}.
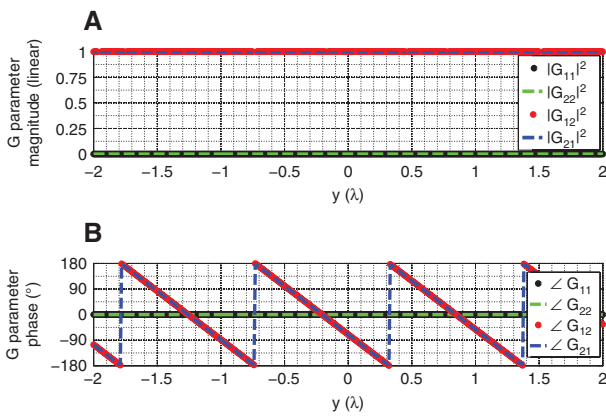
Figure 8: Translated G parameters of bianisotropic boundary conditions for 0° to 71.8° TE refraction at 20 GHz.
(A) Magnitude of G_{11}, G_{22}, G_{12}, and G_{21}. (B) Phase of G_{11}, G_{22}, G_{12}, and G_{21}.

Figure 9: Close-up of a section of the top and bottom sides of the fabricated metasurface for reflectionless refraction at 20 GHz using a three-layer design.
Inset: Example of an asymmetric three-layer unit cell used for the fabricated refracting metasurface.

The fabricated prototype achieved minimal reflections with higher than 80% refraction efficiency of the total scattered power [60]. While this demonstration showed higher than expected losses due to imperfections in fabrication, the obtained refraction efficiency remained clearly higher than what was possible with non-bianisotropic refraction surfaces [41, 60]. A related experimental demonstration of bianisotropic refraction was also presented in Ref. [70], which showed good efficiency for two different cases of refraction (0° to −70° and 20° to −28°) at 10 GHz. The designs, which also utilized the asymmetric three-layer PCB structure, were measured using a near-field setup to obtain the transmission characteristics of the metasurface. While the reflections of the prototype were not characterized, the work in Ref. [70] showed good refraction properties with the use of bianisotropy. The physical realizations hereby described along with previous theoretical designs demonstrate the benefit of utilizing bianisotropic HMSs for applications in wide-angle refraction.
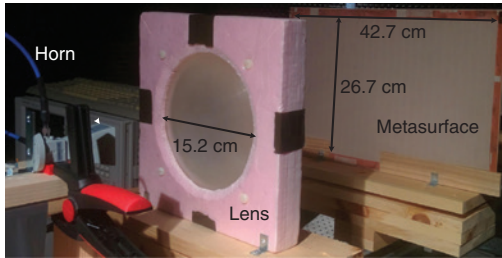
Figure 10: Quasi-optical setup utilizing a Rexolite lens to focus the Gaussian beam pattern of a horn antenna on to the metasurface under test to achieve planar wave illumination, which is used for characterization of the metasurface specular reflections. Obtained from Ref. [60].
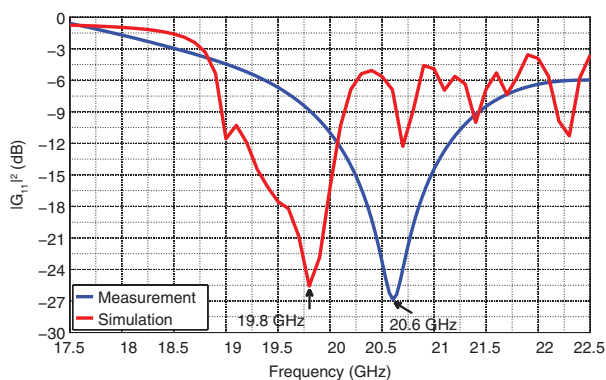
Figure 11: Measured specular reflections of a fabricated reflection-less bianisotropic metasurface for 0° to 71.8° refraction at a frequency band around 20 GHz via a quasi-optical measurement setup. Obtained from Ref. [60].
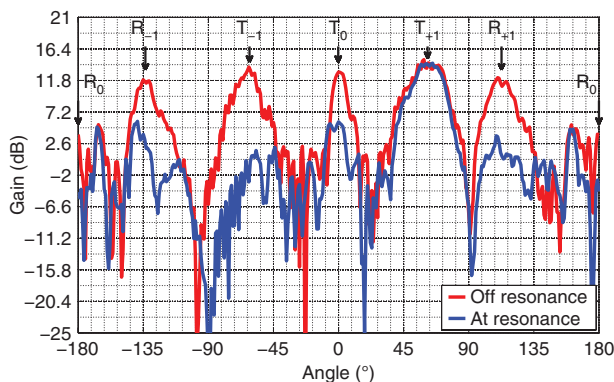
Figure 12: Measured far-field gain pattern (refractive properties) of a fabricated reflectionless bianisotropic metasurface for 0° to 71.8° refraction at 20 GHz. Obtained from Ref. [60].

3.2 Antenna beam forming

In the previous examples of refracting surfaces, the structures were all designed to interact with plane waves.

However, metasurface applications have also been extended to beam forming from arbitrary sources such as in the case of metasurface lenses and antennas [21, 41, 45, 53, 64]. These metasurfaces are often sought after for their applications in antenna systems for directive radiation. Metasurfaces used for these antenna applications can be designed in many ways. In this review article, we will briefly discuss two previously demonstrated methods, namely, the impedance/admittance and the bianisotropic boundary condition (BC) methods. In both methods, a key enabler for allowing an elementary feed antenna to interact with a close-by metasurface is to use the Fourier plane-wave expansion to represent the fields of the feed antenna [42].

The impedance/admittance method utilizes the previously shown non-bianisotropic boundary condition formulation in Eq. (3) to account for any arbitrary excitation source for directive radiation [45, 53, 64]. The fields of the incident and desired output waves can be stipulated and the corresponding surface electric impedance Z_{se} and magnetic admittance Y_{sm} can be found, similar to the refracting and reflecting scenarios [21–23]. A detailed exposition of this method is presented in Ref. [45]. In this formulation, the excitation source may be chosen to be any arbitrary field, which may model real antenna excitations, while the output radiated field is chosen to be a modulated plane wave propagating at a desired angle. By choosing the angle of the output plane wave, the beam of the metasurface antenna can be steered, and by choosing a modulated plane-wave profile, directive radiation is specified. To obtain the required boundary conditions, the incident, reflected, and transmitted fields associated with the source and the desired output beam are first decomposed to their respective plane-wave spectra via the Fourier transform [45]. These spectra at first represent the generalized expressions of the desired waves. To determine the exact spectrum decomposition, however, the reflected, transmitted, and incident fields are then related via the local-power-conservation and the local-impedance-equalization conditions at the metasurface boundary [45]. These conditions are applied to stipulate reactive boundary conditions, meaning that the metasurface would be lossless and passive. Once the full decompositions of the waves are obtained, the boundary conditions necessary for the field transformation can be calculated. Utilizing this method, a cavity excited antenna was designed and demonstrated via fullwave simulations and experimental measurements [53].

The fabricated antenna, which can be seen in Figure 13, displayed high aperture illumination efficiency, low sidelobe level (SLL), and high realized gain. The presence of the cavity helped to illuminate effectively the metasurface
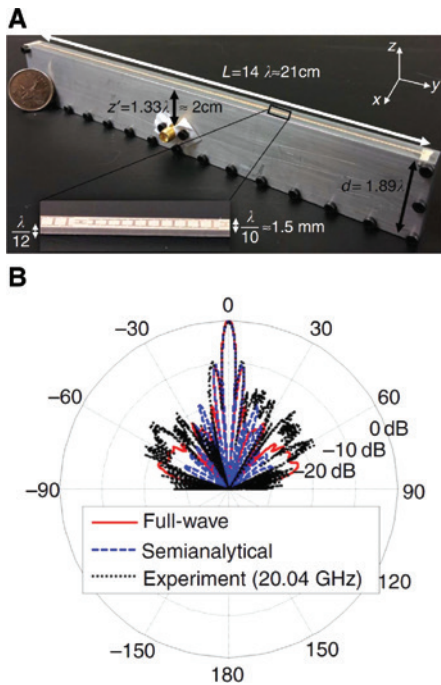
Figure 13: Cavity excited HMS antenna. Obtained from Ref. (53). (A) Photograph of the physical metasurface antenna. (B) Analytical, fullwave, and measured gain pattern of the metasurface antenna.

capability to shape the radiated beam. To enable the synthesis of arbitrary antenna patterns, there is a need to precisely control the local reflection coefficients. In turn, this would enable the metasurface modulation to be arbitrarily designed based on any desired antenna pattern. However, originally, the impedance/admittance method utilized the non-bianisotropic boundary condition formulation. As it was desired to define a purely reactive surface enabled by a local-impedance equalization condition, reflected fields that obeyed Fresnel-type reflection coefficients were required. Thus, the modulation of the metasurface could not be arbitrarily set, which limited the control of the output beam shape [64]. Later, when bianisotropic boundary conditions were introduced through the study of the perfect or reflectionless refraction surfaces, it was shown that this new formulation allows arbitrary control of the local reflection coefficients [42, 54, 55]. Therefore, by applying the bianisotropic boundary conditions to beam-forming metasurfaces, this new formulation would not be restricted by the Fresnel reflections and should allow arbitrary control over the output beam. In this pursuit, the bianisotropic BC method was introduced.

The bianisotropic BC method allowed the tailoring of the metasurface to produce output wave fronts, which are associated with well-known antenna radiation patterns. Applying this method, antenna radiation patterns, which correspond to a Taylor distribution, were demonstrated using fullwave simulations and can be seen in Figure 14

from a small feeding antenna in its close proximity. Apart from the radiation direction and high-aperture efficiency, another desired feature of metasurface antennas is the
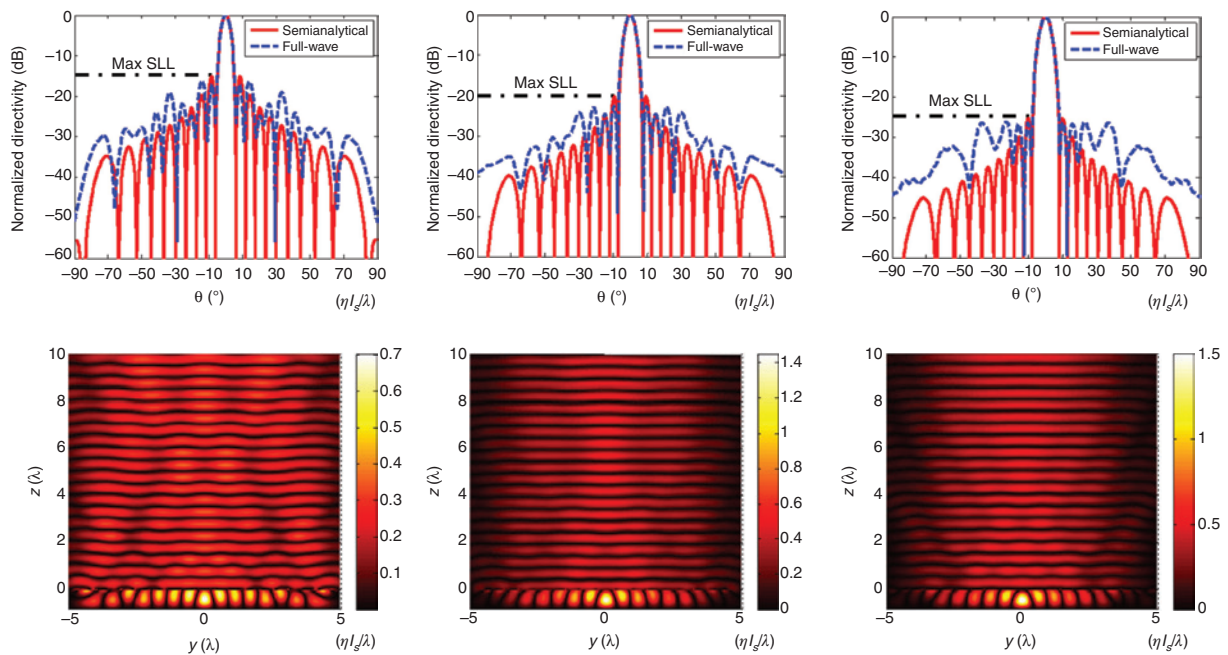
Figure 14: Fullwave simulations of cavity excited bianisotropic HMS antenna for Taylor distribution showing controllable side lobe levels. Obtained from Ref. [64].

[64]. By varying the desired distribution, different radiation patterns with varying SLLs were presented using the same design methodology. In addition, the same design approach has been used for demonstration of binomial and Dolph-Chebyshev distributions, which exhibited good agreement with the expected antenna radiation profiles [65]. Utilizing the bianisotropic BC method, various examples of arbitrary beam shaping have been demonstrated, which validates the capability for HMSs to arbitrarily shape beam patterns for antenna applications. In addition, this method further emphasized the advantage of using bianisotropy in metasurface designs.

3.3 Perfect reflection

Somewhat surprisingly, recent developments have shown that it is highly non-trivial to arbitrarily reflect an incident wave with perfect efficiency. The following perspective helps us understand why: in Section 3.1, we showed that perfect transmission in a metasurface is achieved by using a multilayer surface to match the impedances of the input and output waves. However, for a reflective metasurface, the incident and reflected waves share a half-space and are hence superimposed atop each other. Hence, when their wave impedances differ, simple impedance matching techniques cannot be applied to reflect the wave with perfect efficiency. Consider a perfect TE anomalous reflection metasurface shown schematically in Figure 15. Recent works have found that above a perfect anomalous reflection surface, the normal Poynting vector, which represents power flow into or out of the metasurface, fluctuates in a sinusoidal fashion [55, 58, 71]:

$$\Re\{S_z\} = \frac{|E_{x,i}|^2}{2\eta_0} \sqrt{\max\left(\frac{\cos\theta_i}{\cos\theta_r}, \frac{\cos\theta_r}{\cos\theta_i}\right)} \\ \cdot (\cos\theta_r - \cos\theta_i)\cos(k_g(y - \phi))$$ (6)

Here the surface runs along the *xy*-plane and anomalous reflection happens in the *y*-direction. $E_{x,i}$ is the incident
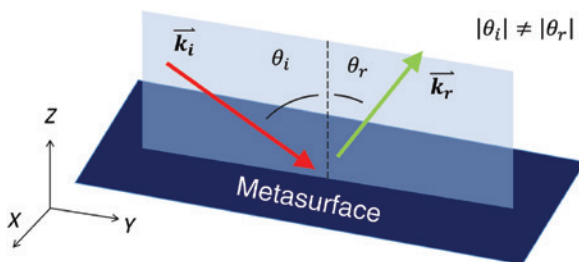
Figure 15: A schematic diagram of a perfect anomalous reflection metasurface.

electric field, η_0 is the characteristic impedance of free space, $k_g = 2\pi/\lambda_g$ is the metasurface's spatial frequency, λ_g is its period of variation, θ_i and θ_r are the incidence and reflection angles, and ϕ is a phase shift upon reflection from the metasurface. We see that, aside from specular reflection ($\theta_r = \theta_i$) and retroreflection ($\theta_r = -\theta_i$), (6) assumes a sinusoidal variation along the *y*-direction. Hence, half the area of the surface must be lossy (reradiates less power than is incident upon it) while the other half must be active (reradiates more power than is incident upon it). Lossy metasurfaces can be implemented with relative ease, but they reduce the metasurface's power efficiency; active metasurfaces represent a level of complication best to be avoided. This dilemma hence hindered, until very recently, the demonstration of perfect anomalous reflection with a metasurface.

The earliest reflection metasurfaces redirected an electromagnetic wave by applying a linear phase shift upon reflection. It has been shown that, besides obtaining a reflected beam in the desired direction, such surfaces also diverted some power to spurious reflected directions. It was shown [55, 72] that for such surfaces, the maximum power efficiency is as follows:

$$\eta = \frac{4\cos\theta_i \cos\theta_r}{(\cos\theta_i + \cos\theta_r)^2}.$$ (7)

The spurious reflection components can be eliminated if one can tailor both the amplitude (from 0 to 1) and phase (from 0 to 2π) of the reflection coefficient. Reference [49] demonstrated an HMS that achieves the necessary tuning; Ref. [55] and [58] calculated the necessary (lossy) impedance profile that allows one to perform anomalous reflection without reradiating spurious reflection components. However, in this case, the maximum achievable power efficiency worsens, to the following:

$$\eta = \min\left(\frac{\cos\theta_i}{\cos\theta_r}, \frac{\cos\theta_r}{\cos\theta_i}\right).$$ (8)

Most recently, study on this topic has led to a class of "non-local" metasurfaces, which can redistribute power along the metasurface to satisfy (6). Reference [63] first showed this functionality by exciting auxiliary evanescent standing waves along the metasurface, which facilitated a rapid power fluctuation that satisfied (6), hence leading to perfect power transfer from the incident to the reflected wave. Reference [73] achieved power redistribution through a leaky-wave based metasurface design – the wave incident to the "lossy" region of the metasurface is somewhat absorbed by the leaky wave; this absorbed power then propagated briefly along the metasurface

and was re-radiated in the "active" region of the metasurface. Reference [74] also showed that this redistribution could be achieved without resorting to non-local effects if one physically curved the metasurface along a trajectory where the Poynting vector remained constant. The operations of these perfect anomalous reflectors have been verified experimentally and/or numerically. However, the design and fabrication of these surfaces are rather complicated due to the sensitivity of leaky and evanescent waves, the metasurfaces' requirement for deeply subwavelength and/or multilayer elements and for [74] the curvature of the metasurface.

On a parallel front, another group of researchers demonstrated perfect anomalous reflection through a strikingly different paradigm. Whereas most works heretofore on metasurfaces focused on tailoring a continuous impedance profile, a few recent works examined the metasurface as a discrete structure that engineers the diffraction of waves. Prior to the advent of metasurfaces, researchers studying retroreflection from gratings found that some thick gratings could reflect waves at anomalous, or "off-Bragg", angles, with very high efficiency [75–77]. A theoretical investigation from the perspective of plane-wave diffraction showed that perfect anomalous reflection was possible from such structures when two angular parameters can be achieved, for example, by tuning the depth of the grooves in a rectangular groove grating [78]. A recent work from our group, discussed later in this section, explains why a conceptually simple device such as a grating may achieve the power redistribution described in (6). More recently, Ra'di et al. [79] proposed the concept of "meta-gratings". This work, through diffraction calculations and numerical investigation, demonstrated that when electric and magnetic current pairs were properly spaced from each other and from the ground plane below them, the interference characteristics canceled re-radiation from the specular direction and thereby allowed one to transfer all the power into the anomalous direction. Reference [80] presented an analytical investigation on a metagrating built from an array of dipoles and demonstrated their use toward the design of perfect reflection beam splitters, which also required a redistribution of power along a metasurface, in a similar fashion to (6). These works provide exciting insights to constructing anomalous reflection metasurfaces; they show the potential of achieving wave manipulation properties using discrete meta-scatterers.

We have experimentally demonstrated perfect anomalous reflection using a discrete HMS without a tunable thickness. Our concept of the discrete HMS is to take the discrete nature of the metasurface into account from the initial design phase. Specifically, when one considers a reflection metasurface as a surface that is spatially discrete and periodic, the reflection profile in spectral (spatial frequency) domain is that of a train of delta functions, as shown in Figure 16. Here diffraction orders are separated by $k_g = 2\pi/\lambda_g$, where λ_g is the grating period. In general, each diffraction order has a unique reflection amplitude and phase. Let N denote the number of diffraction orders within the propagation range (i.e. $k \in [-k_0, k_0]$). This number can be upperbounded, i.e. $N \leq 2k_0/k_g$. We have shown that, in order to tune arbitrarily the amplitudes and phases of each propagating diffraction order, one needs to discretize each period of the metasurface into at least N elements. In this paradigm, specular reflection, which obeys the reflection law $\theta_r = \theta_i$, is represented by the zeroth diffraction order. We achieve anomalous reflection by (i) tuning the metasurface period to steer the first (or minus first) diffraction order into the desired direction and thereafter (ii) maximizing the amplitude of that diffraction order. We find that in many cases, k_g is sufficiently large, such that $N = 2$. In these cases, metasurface design and fabrication are dramatically simplified to a structure featuring two cells per grating period. We call this structure a binary HMS.

To demonstrate the binary HMS paradigm, we first used it to design a near-perfect retroreflector for an electromagnetic wave at near-grazing incidence [81, 82]. This was a special case of anomalous reflection where, as obtainable from (8), power reflection with perfect efficiency can be achieved by conventional blazed gratings [83]. Nonetheless, the binary HMS made a robust, low-profile, and efficient retroreflector for this application. For this work, we chose as the metasurface element an electric dipole backed by a dielectric spacer and a metallic ground plane, as depicted in Figure 17A. In a prior work [49], we showed how this simple element functioned as a passive Huygens' source and that its operation extended from microwave to optical frequencies. Figure 17B shows that by varying the length of the dipole element, we realized a
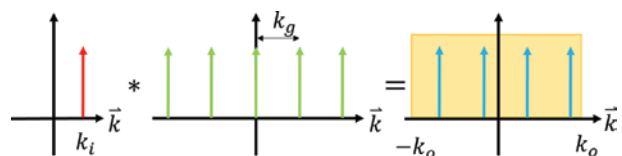
Figure 16: A diagram showing spectral representations of the illumination wave (left), the periodic metasurface (center), and the reradiated wave (right). The arrows represent the presence of a plane wave/diffraction order but do not imply uniform amplitude or phase across the diffraction orders.
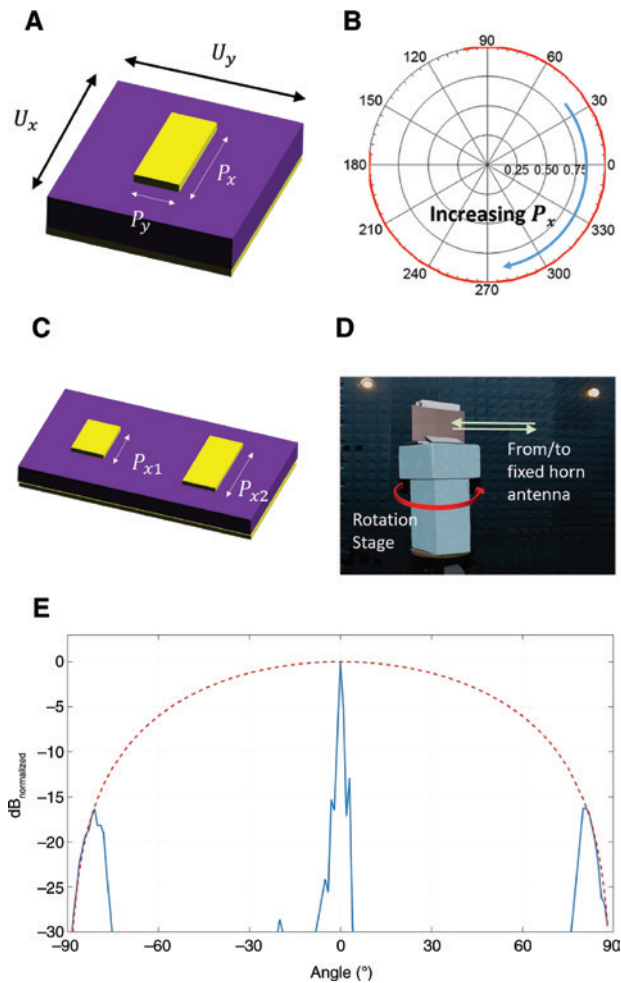
Figure 17: Design and experiment of the retroreflection BHM. Obtained from [82].
(A) A diagram of the ground-backed dipole element. Yellow represents metal (copper), and purple represents the substrate (Rogers RT Duroid 5880, $\varepsilon_r = 2.2$). (B) The variation in reflection coefficient as the dipole length P_x is swept. (C) A period of the dipole formed by placing two metasurface elements adjacent to one another. (D) A photograph of the experimental apparatus where the monostatic RCS is measured. (E) The measured monostatic RCS for TE retroreflection BHM.

phase tuning range of nearly 360°. We chose two element lengths, which gave reflection phase shifts that differ by 180°, and placed them adjacent to one another to form the elements of the binary HMS. Figure 17C shows a period of the resultant metasurface. This arrangement should provide total suppression of the specular reflection mode and hence redirect the incident wave into retroreflection with perfect efficiency. After slight length adjustments to account for coupling effects between these elements, the resultant metasurface achieved a highly efficient retroreflection for an incident wave at $f = 24$ GHz and $\theta_i = 82.87°$. Figure 17D shows the metasurface mounted on a rotation stage in a far-field antenna chamber. A horn antenna to

the right of the photo illuminates the metasurface and receives the retroreflected wave. As the metasurface rotates with its stage, the retroreflected signal strength is measured as a function of the incidence angle. This hence forms a monostatic radar cross-section (RCS) measurement for the metasurface, which we show in Figure 17E. As expected, we measured strong retroreflection signals at normal incidence as well as ±82°, where we obtained a retroreflection power efficiency of 94% in simulation and 93% in experiment. While this surface retroreflects a TE-polarized wave, we designed an analogous surface with slots replacing dipoles to retroreflect a TM-polarized wave, with similar power efficiency (99% in simulation, 93% in experiment).

Following the same methodology, we designed a binary HMS that achieved perfect anomalous reflection at 24 GHz [71, 84]. This metasurface was designed to accept an incoming plane wave at $\theta_i = 50°$ and reflect it to $\theta_r = -22.5°$. The unit cell and single period architecture for this metasurface is the same as that for the retroreflection metasurface, shown in Figure 17A and C. Table 1 tabulates the material and feature dimensions for this binary HMS. A (periodic) Floquet simulation showed that this metasurface performed the desired anomalous reflection with 99.98% efficiency, which was perfect within the tolerance of the simulation. Figure 18A plots the incident and reflected (scattered) waves as calculated by the simulation software. We then truncated the metasurface to 78 cells (413.4 mm) and simulated its scattering pattern across a range of frequencies. Figure 18B (top panel) shows the simulated scattering pattern for the binary HMS at 20 GHz, compared with that of a perfect conductor of the same size. Clearly, power from the incident wave was completely redirected into the anomalous direction of $\theta_r = -22.5°$. Figure 18B (bottom panel) shows the same comparison over a range of frequencies, from 22.0 GHz to 28.5 GHz. We observed beam squinting (the variation of

Table 1: Specifications and key dimensions for the perfect anomalous reflection binary HMS.

Specifications	
Operation frequency	24 GHz
Operation angles	$\theta_i = 50°; \theta_r = -22.5°$
Printed circuit board	
Substrate	Rogers RT/Duroid 5880
Thickness	1.575 mm
Dielectric constant	2.20 ± 0.02
Dielectric loss	$0.0004 \leq \tan\delta \leq 0.0009$
Key design dimensions (see Figure 17)	
$U_x = U_y = 5.44$; $P_{x1} = 2.0$; $P_{x2} = 3.6$; $P_y = 1.5$ (all units in mm).	
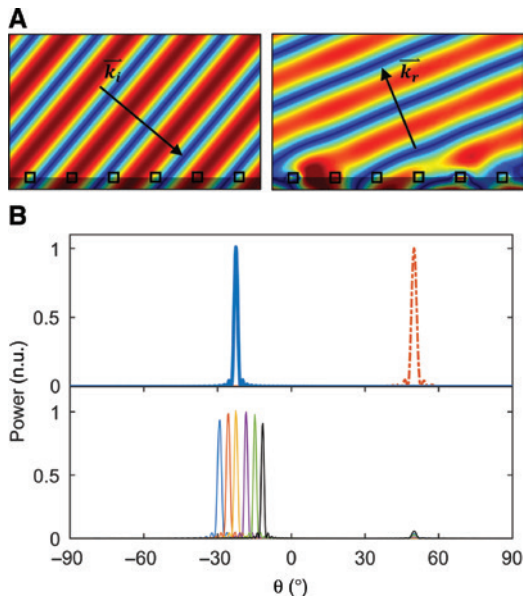
Figure 18: Full-wave simulation of the anomalous reflection BHM.
(A) Electric field magnitudes of the incident (left) and scattered (right) waves. The shaded area denotes the metasurface, black boxes denote the location of the dipoles. Obtained from [71]. (B) Top panel: simulated scattering for truncated BHM (blue, solid), compared alongside that for a metallic plate with the same size and shape (red, dashdot). Bottom panel: same as the top panel but over a wide bandwidth. Displayed frequencies are (left to right) 22 GHz, 23 GHz, 24 GHz, 25.5 GHz, 27 GHz, and 28.5 GHz. Obtained from [71].

Figure 19: Experimental demonstration of the anomalous reflection BHM.
(A) A close-up of the fabricated BHM. Obtained from [71]. (B) A photograph of the experimental apparatus, showing the transmit (Tx) and receive (Rx) antennas, as well as the metasurface. Obtained from [71]. (C) The measured bistatic RCS (blue, solid), compared alongside that for a metallic plate of the same size and shape (red, dashdot). Obtained from [71].

beam angle with respect to frequency), as was common with various antenna arrays and reflect arrays. Notwithstanding this, the non-resonant nature of the design allows the BHM to perform high-efficiency anomalous reflection. An efficiency surpassing 90% was achieved over this 25.7% bandwidth. Figure 19A shows a close-up of the fabricated metasurface; Figure 19B shows the experimental apparatus we used for its characterization. From the right, a lens antenna launched a 24-GHz wave toward the metasurface at $\theta_i = 50°$ from a distance of 1.5 m. A second lens antenna equidistant from the metasurface measured the scattering. This receive antenna was rotated to measure the bistatic RCS of the metasurface upon the prescribed incidence. Figure 19C compares the bistatic RCS of the BHM with that of a metal plate of the same size and shape. The experimental results agree well with simulation: specular reflection was suppressed by 20 dB compared to the metal plate, and near-perfect anomalous reflection was achieved.

To investigate how this apparently simple metasurface achieved the power redistribution required in (6), we examined the electromagnetic field and power flow normal to selected planes parallel and in close proximity to the metasurface. We observed strong evanescent

electromagnetic fields existed at subwavelength distances from the metasurface. Most likely, this strong evanescent component performed similarly to auxiliary waves proposed in Ref. [63]. However, their implicit existence in a much simpler structure boded well for the broadband operation of the perfect anomalous reflection BHM and its practicality for scaling up to millimter-wave and THz frequencies. This discovery also provided one plausible explanation on how some grating structures demonstrated near-perfect anomalous reflection notwithstanding the recently discovered requirement (6).

3.4 Review of optical HMSs

At optical frequencies, the difficulty in obtaining magnetic response and the inevitable high Ohmic loss have been the main bottlenecks in early optical HMS research. As such, various "Huygens'-like" metasurfaces that utilize multiple layers of admittance sheets have been initially demonstrated for which some of these metasurfaces are shown in Figure 20A–C [23, 51, 85]. Here a key Huygens' property (i.e. properly weighted orthogonal electric and magnetic induced currents) can be conceptually
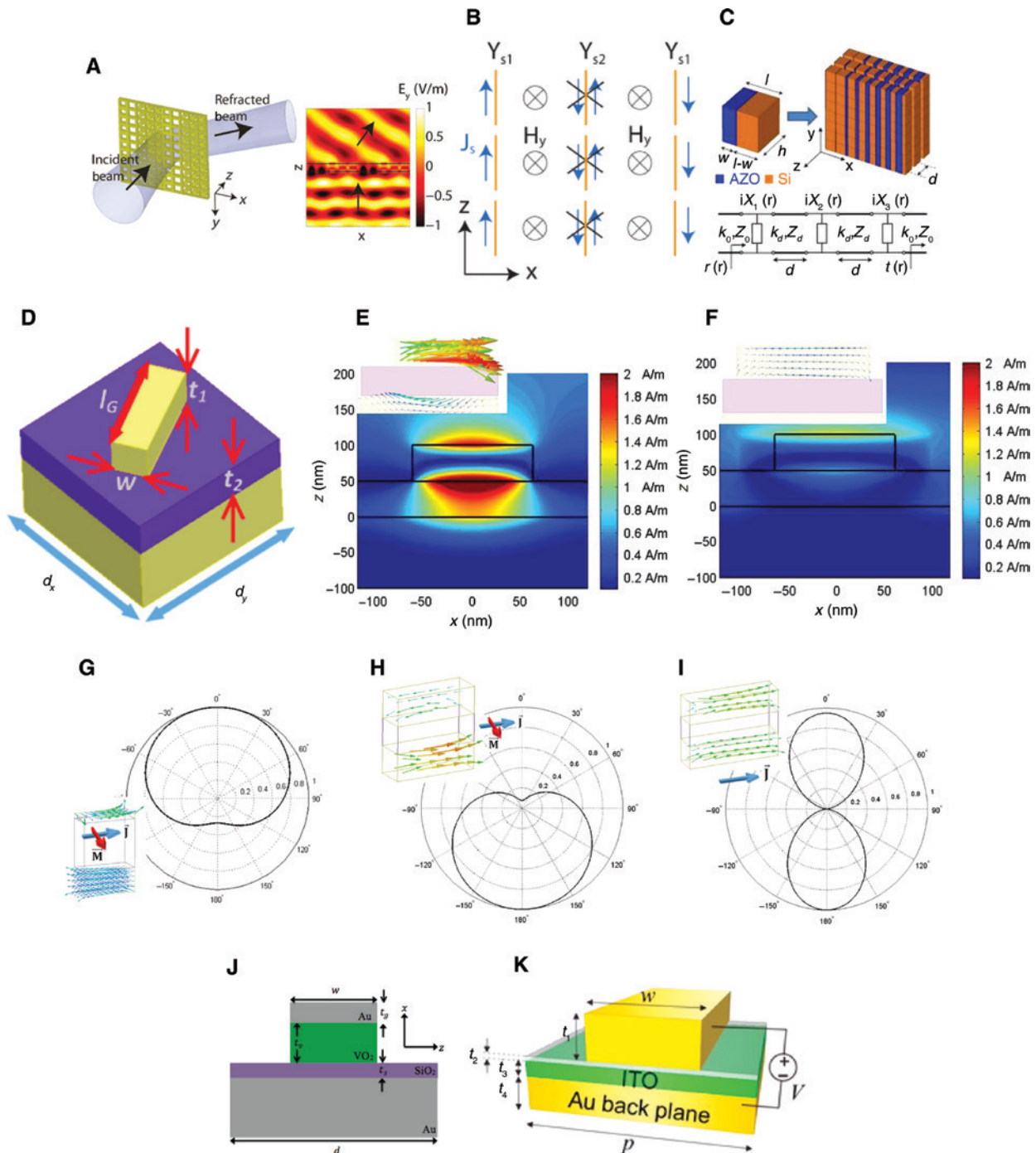
Figure 20: Metallic optical Huygens' metasurfaces.

(A) The Huygens'-like metasurface that arbitrarily refracts an incident field (obtained from [51]) and (B) its induced currents within the layers (obtained from [85]). (C) Another Huygens-like metasurface and its equivalent circuit model (obtained from [23]). (D) The gap-surface plasmon resonators that comprise optical HMS and their equivalent circuit model (obtained from [49]). Magnitude profiles of the y component of the magnetic field inside one infinitely periodic GSP resonator, when the length of the nanorod is (E) 125 nm and (F) 200 nm. The other geometrical parameters are taken from Ref. [49]. The insets show corresponding induced current distribution. The radiation patterns of a unit cell that is electromagnetically similar to the gap-surface plasmon resonators when it is scattering in (H) the backward, (G) the forward, and (I) both directions (obtained from [49]). The insets show the induced current distribution upon normal plane wave incidence at 800 nm. The widths and lengths of the nanorods and silica in (H) are set to 50 nm×110 nm, respectively, while the thicknesses for the silica, top, and bottom nanorods are, respectively, set to 100 nm, 10 nm, and 50 nm. The dimensions of the two gold nanorods and silica spacer in (G) and (I) are (G) 50 nm×50 nm×200 nm and (I) 50 nm×50 nm×140 nm. The reconfigurable gap-surface plasmon resonators that utilize (J) vanadium dioxide (obtained from [86]) and (K) indium tin oxide as phase changing materials (obtained from [87]).

envisioned by considering the effect of an incident electric and magnetic field separately. Specifically, an incident electric field would induce electric currents in all layers while an incident magnetic field would excite anti-parallel currents in the outermost layers that result in magnetic current (Figure 20B). The directions of these induced electric and magnetic currents are orthogonal to each other; hence, they mimic the Huygens' property. Despite such a conceptual Huygens' interpretation, however, they closely resemble transmitarrays and their method of analysis indeed follows that of transmitarrays at microwaves. For example, Monticone et al. [23] have analyzed their Huygens'-like metasurfaces by modeling each layer as a shunt reactive network separated by a transmission-line segment, thereby determining the required surface reactances in each layer. Their analysis has also established that electrical responses alone from each layer sufficed to synthesize arbitrary reflection and transmission properties. See also related discussion surrounding Figure 4. These Huygens'-like metasurfaces operate in the transmission mode, and their transmission efficiencies are mainly limited due to plasmonic Ohmic loss (e.g. 30% power transmission efficiency was reported in [51]).

On the other hand, high-efficiency optical Huygens' metasurfaces (OHMs) have been demonstrated, which operate in the reflection mode [49, 88–90]. Figure 20D shows the so-called gap-surface plasmon (GSP) resonators, which have been used as unit cells in these OHMs. They take advantage of a metallic back plate for efficient light reflection, while the metallic nanorods spaced by a dielectric layer provide necessary electric and magnetic currents for synthesizing the surface currents in Schelkunoff's equivalence principle [49]. Here, an incident electric field is polarized along the nanorods, which would induce electric currents in the nanorods and the substrate. On the other hand, an incident magnetic field would induce circulating electric currents in the nanorods and the substrate, thereby generating a magnetic current. This is illustrated in Figure 20E and F. In particular, Figure 20E shows strongly enhanced magnetic field between the nanorods and the substrate, as the field would be in a typical Fabry-Perot resonator. In such a case, unequal and opposite electric currents are induced in the nanorods and the substrate (inset in Figure 20E), which indicates simultaneous existence of both electric and magnetic currents. On the contrary, when the nanorods are not properly tuned, the field is no longer confined and the induced current is mostly confined within the nanorods, as shown in Figure 20F. As a further illustration, the radiation patterns of single isolated unit cells that are electromagnetically similar to the GSP resonators are shown in Figure

20H–I. In this isolated cell analysis, the dielectric layer and the ground plane are truncated to match the size of the nanorod, as the purpose is to simulate a single unit cell that is not coupled. The geometrical parameters are set similar to the GSP resonators at an operational wavelength of 800 nm (see the caption of Figure 20H–I for details). It is seen that the radiation patterns are unidirectional for certain resonator lengths, which is a unique property of a Huygens' unit cell and demonstrates the simultaneous existence of orthogonal electric and magnetic dipoles. Specifically, when a magnetic current is absent, they scatter in both the forward and backward directions, while they scatter either in the forward or the backward direction in the presence of both electric and magnetic currents.

Based on the GSP resonators, anomalous reflection, asymmetric beam splitting, far-field pattern engineering, focusing, birefringence polarization control, and holograms have been demonstrated [49, 88–91]. In particular, the demonstrations in Ref. [49] have established that the surface needs a user-designed spatially varying reflection loss in addition to surface reactance for complete reflected wavefront control (in particular, for controlling the amplitude of the reflection coefficient). In this respect, the authors have deliberately introduced polarization losses into their surfaces by rotating the gold nanorods with respect to the incident polarization vector, thereby designing passive and lossy OHMs. However, as pointed out by Asadchy et al. [55] and Epstein and Eleftheriades [63] the efficiency of such a lossy and reactive surface is not unity. In this regard, the topic of perfect reflection/refraction has gained much attention recently, as was previously discussed. Following the introduction of passive OHMs, their reconfigurable version has also been demonstrated [86, 87]. Instead of utilizing non-tunable materials (e.g. silica) that are placed between the gold nanowires and the substrate, these reconfigurable metasurfaces employ vanadium dioxide (VO_2) or indium tin oxide (ITO) as the phase changing materials. For the VO_2-based structure, a DC current is applied to the gold nanowire, which in turn increases the temperature of VO_2 and induces its insulator-to-metal phase transition. This enables the unit cell's reflection coefficient to be dynamically tuned based on the state of VO_2. On the other hand, a DC voltage is applied between the gold nanowire and the metallic back plate for the ITO-based surfaces. This changes the refractive index of ITO in a unit cell, thereby altering its reflection coefficient.

In an effort to further minimize the Ohmic loss, all-dielectric OHMs have also been demonstrated. The fundamentals of these all-dielectric Huygens' unit cells have

been established by the early works of Mie, Lewin, and Kerker et al. [92–94]. The former has established the connection between the scattering properties of a dielectric structure to its electric and magnetic multipole coefficients [92]. This allows the backward (Q_{bs}) and forward (Q_{fs}) scattering efficiencies to be expressed in terms of electric (a_m) and magnetic (b_m) multipole coefficients given by [95],

$$Q_{bs} = \frac{1}{k^2 r^2} \left| \sum_{m=1}^{\infty} (-1)^m (2m+1)(a_m - b_m) \right|^2$$

$$Q_{fs} = \frac{1}{k^2 r^2} \left| \sum_{m=1}^{\infty} (2m+1)(a_m + b_m) \right|^2$$

(9)

On the other hand, Lewin [93] has formulated the effective permittivity and permeability of a material loaded with spherical particles, while Kerker et al. [94] have shown that a dielectric sphere with equal electric permittivity and magnetic permeability possesses zero backscattering and no depolarization. Such properties are similar to those of a Huygens' source, and it is known as the first Kerker condition. For example, Figure 21 shows a scattered radiation pattern of a nanosphere that satisfies this condition. The observed pattern is unidirectional (a cardioid pattern) and radiates either in the forward or in the backward direction similar to the pair of GSP resonators (Figure 20H and G). The first Kerker condition corresponds to the case where the electric and magnetic multipoles have equal coefficients in which the zero backscattering can also been seen from (9) for $a_m = b_m$. In light of the first Kerker condition, dielectric nanoparticles of various shapes (spheres, cubes, cylindrical disks, and rods) have been investigated to engineer their forward/backward scattering properties for certain functionalities [97–101]. In particular, Cheng et al. and Decker et al. have
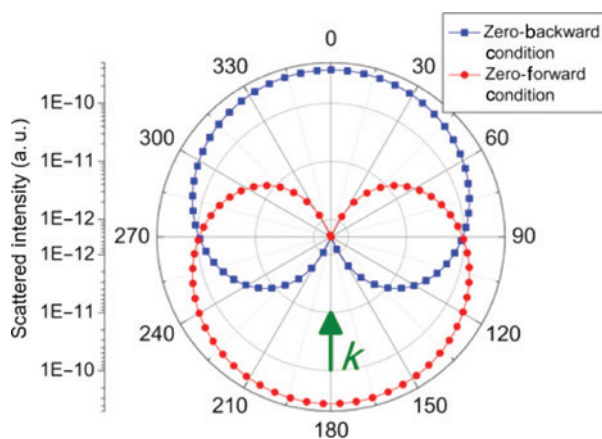
Figure 21: A cardioid radiation pattern from a nanosphere that satisfies the first Kerker condition (obtained from [96]).

demonstrated zero backscattering with an array of silicon nanodisks that also offer full 2π transmission phase by spectrally overlapping electric and magnetic dipole resonances [102–104]. Figure 22C shows the transmission properties of silicon nanodisks when the electric and magnetic dipole resonances are separated and collocated. Specifically, when they are collocated, the transmission magnitude is unity, while the transmission phase offers full 2π variation. Subsequent works by numerous researchers have utilized such an idea and similar inclusions to demonstrate various wavefront manipulations, ranging from THz to visible wavelengths [105–128]. For example, Figure 22D and E shows arbitrary beam refraction and focusing with an array of silicon nanodisks [105]. Such functionalities have also been demonstrated with similar dielectric inclusions, and regardless of the shape of the unit cells being used, the common goal is to parametrically characterize them and utilize a set that provides full 2π phase variation with maximized transmission magnitude. This is to implement a certain phase profile that is deduced from the generalized Snell's law. On the other hand, Shanei et al. [106] have demonstrated beam focusing with desired full width half maximum (FWHM) and SLL based on an array of silicon nanoblocks. To achieve arbitrary FWHM and SLL, however, both phase and magnitude modulation must be simultaneously applied on unit cells [49]. While the proposed silicon nanoblocks do not offer complete/systematic independent control over the phase and magnitude, the work in Ref. [106] presents parametric characterization results as a function of transmission magnitude and phase. From these results, certain geometries of unit cells are selected, which feature the nearest values to the required ones, as shown in Figure 22F. Figure 22G shows another type of all-dielectric unit cells [107]. These metasurfaces are, strictly speaking, not HMSs, as they rely on the waveguiding effect (i.e. phase accumulation) for achieving 2π phase shift. As such, their height should be tall enough to cover a 2π transmission phase. The variation in local phase accumulation is obtained by having a variable proportion of dielectric within a period (i.e. mixing of materials that results to certain effective local mode index). However, Kruk et al. [129] have recently demonstrated Huygens' property as represented by Figure 21 with similar unit cells (nanopillars). Instead of viewing them as local waveguides, the authors have engineered the heights and other geometrical parameters of nanopillars to employ higher order electric and magnetic multipoles (in addition to electric and magnetic dipoles) for better suppression of backward scattering waves and enhanced forward scattering. Another Huygens'-related metasurface is shown in Figure 22H, which employs an
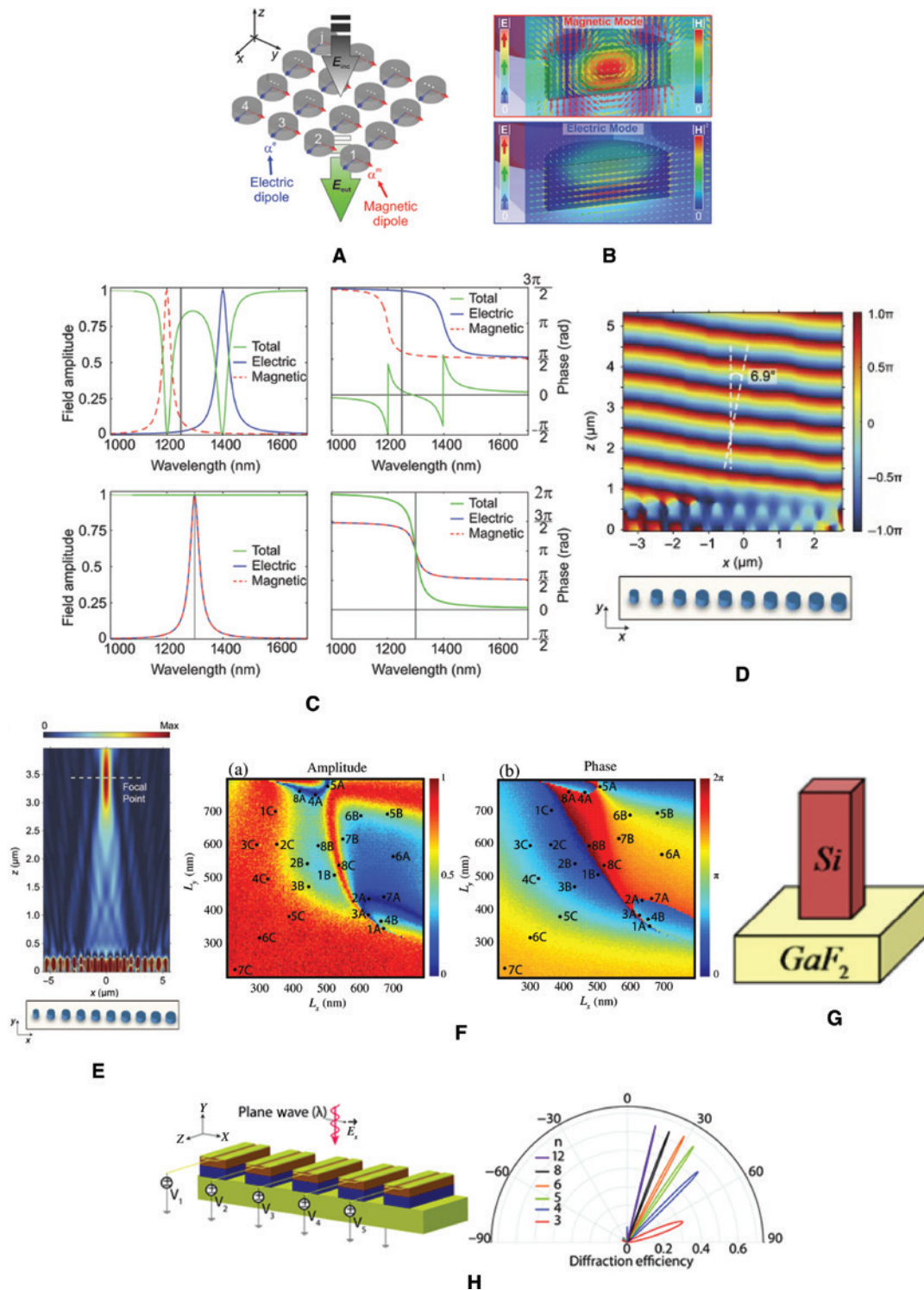
Figure 22: All-dielectric optical Huygens' metasurfaces.
(A) An array of silicon nanodisks that forms an all-dielectric optical HMS (obtained from [103]) and (B) the corresponding electric and magnetic dipole modal profiles (obtained from [103]). (C) The transmission amplitude and phase variations that demonstrate the effect of separating/collocating the electric and magnetic resonances (obtained from [103]). The demonstration of (D) arbitrary beam refraction and (E) focusing with an array of silicon nanodisks (obtained from [105]). (F) The variation of transmission magnitude and phase as a function of lengths (L_x) and widths (L_y) of a silicon nanoblock and the design points that are used for constructing a focal spot with desired FWHM and SLL (obtained from [106]). (G) An optically tall all-dielectric unit cell that utilizes waveguiding effects for obtaining 2π phase shift (obtained from [107]). (H) A reconfigurable metasurface that dynamically engineers magnetic dipole resonance of InSb blocks that sit on a metallic backplate for dynamic reflected wavefront manipulation (obtained from [108]).

array of indium antimonide (InSb) nanoblocks that are directly placed on a metallic backplate [108]. The overall system can be interpreted as an array of reconfigurable magnetic dipoles on a metallic backplate. To obtain the reconfigurability, a metallic contact is deposited on InSb, as shown in the figure. This allows dynamic alteration of magnetic dipole resonance of the InSb blocks depending on the biased voltage such that the local reflection coefficients can be reconfigured.

3.5 Active HMSs

Heretofore in this paper, we have examined various kinds of HMSs, which manipulate incoming waves in a passive manner to achieve a desired output waveform. In this section, we review works on active HMSs and their applications. Ample works exist in the literature on the topic of *active-controlled* metasurfaces [130–141]. These works modify an inherently passive metasurface by injecting an auxiliary signal thermally, optically, or electrically to change the refractive index, the conductivity, or the material phase at selected locations on the metasurface. At radio frequencies, tunable and/or switchable electrical components, such as varactors and p-i-n diodes, are also used to allow one to tune a metasurface element through voltage bias lines. The aforementioned active tuning schemes change the reflection and transmission phases, loss characteristics, and metallization patterns of the metasurfaces and hence make the metasurfaces highly reconfigurable. Some devices built from such active-controlled metasurfaces include anomalous reflectors, elliptical polarizers, switchable reflectors, absorbers, wave plates, reconfigurable lenses, and frequency-tunable devices.

However, the objective of this section is devoted to HMSs featuring impressed Huygens' source elements. Figure 1 illustrates the general concept of an HMS: an incident (primary) wave generates electric and magnetic currents along the metasurface, which become Huygens' (secondary) sources as they re-radiate the energy into the surrounding media, thus superimposing with the incident wave to form a desired electromagnetic field ($\vec{E}_1$, $\vec{H}_1$) and ($\vec{E}_2$, $\vec{H}_2$). Whereas passive HMSs generate the necessary electric and magnetic currents by manipulating the incident wave with a surface of varying but passive impedance, active HMSs can directly synthesize the required currents through an appropriate feeding network. Compared with its passive counterpart, few works to date have explored the physics and technology of active HMSs. Nonetheless, the vast wavefront engineering potential afforded by such surfaces has been alluded to in several works on planar

metasurfaces. For example, our work on the optical HMS [49], as well as more recent theoretical works [55, 58], discussed the possibility of arbitrarily shaping and/or redirecting an electromagnetic wave with an active HMS.

An extremely intriguing application of an active HMS is that of an active surface invisibility cloak. While the first proposals of electromagnetic cloaks [142, 143] involved a passive metamaterial shell with exotic electromagnetic properties, it soon became apparent that such cloaks came with three disadvantages: (i) they had appreciable losses, which led to imperfect cloaking; (ii) they were inevitably large and heavy (the thickness of the cloak was comparable to the size of the cloaked region); and (iii) their achievable bandwidths were inevitably limited due to the sum rule on the extinction cross-section [144]. In principle, one may overcome all three limitations with an active electromagnetic cloak. It was first proposed in the realm of acoustics [145] and scalar optics [146] that, through exciting active sources surrounding (or partially surrounding) an object, one could cloak an object by suppressing its scattering. In similar spirit, one could also disguise the object into a decoy by altering its scattered signal [147]. Such active cloaks were desirable in that they could be arranged in an ultrathin layer and had potential to be a broadband, thus bypassing requirements for achieving stringent material parameters over a broad bandwidth.

A few years ago, the design and full-wave simulation of the first active electromagnetic cloak have been reported in Ref. [27]. Figure 23 shows a diagram for the operation of this active cloak. Essentially, the active Huygens' cloak has been designed such that, in the presence of the object (a dielectric cylinder), the cloak's impressed currents generated a secondary scattered field, which formed perfect destructive interference with the primary scattered field caused by the incident plane wave. Hence, this suppressed scattering from the object and effectively concealed it. The calculated necessary electric and magnetic currents from the desired free-space fields are given by (10) the following:

$$\vec{M}_s = \hat{n} \times \vec{E}_i, \quad \vec{J}_s = -\hat{n} \times \vec{H}_i \qquad (10)$$

where the subscript *i* denotes incidence, the subscript *s* denotes electric/magnetic surface currents, and $\hat{n}$ denotes the outward pointing normal vector for the closed surface. This set of fields can be interpreted as the negative of the currents, which are equivalent to the incident illumination (induction theorem [25]).

Figure 24A–B displays the fullwave simulation results showing the successful cloaking of a dielectric cylinder. The cloak surrounded a dielectric cylinder with $\varepsilon_r = 10$,
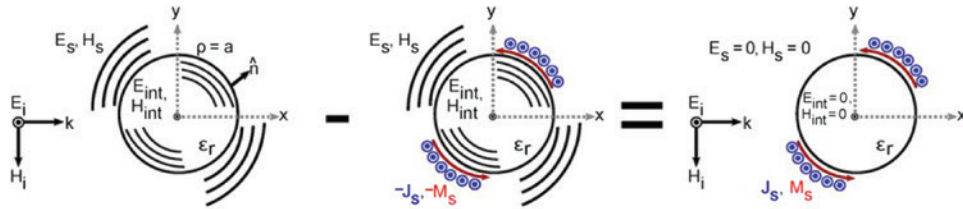
Figure 23: Schematic explanation for the active Huygens cloak.
Left: scattering of a plane wave off a cylindrical dielectric piece. Middle: scattering off the same object, with the incident plane wave replaced by an equivalent set of electric and magnetic currents surrounding the object. The scattered waves were the same for the left and middle scenarios. Right: the destructive interference of scattered waves was facilitated by implementing a cloak with the negative of the aforementioned equivalent currents. Obtained from Ref. [27].
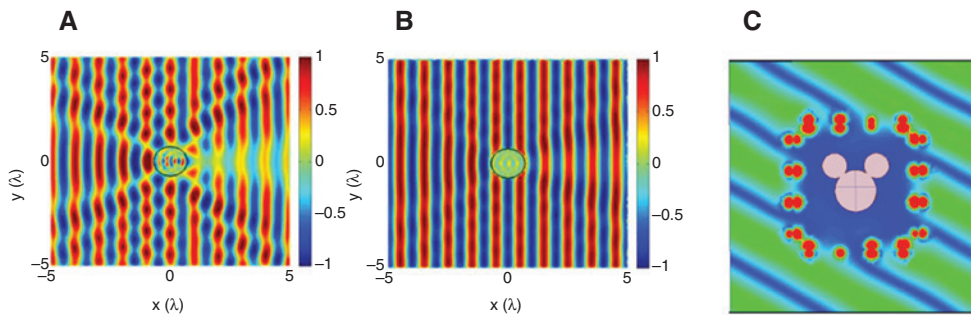
Figure 24: Fullwave simulation results for active cloaking HMS.
(A) Total electric field (real part) of a scattering experiment involving the dielectric cylinder. Obtained from [27]. (B) Same simulation as (A) but with the cloak turned on. Obtained from [27]. (C) Scattering cancellation for a square-shaped cloak concealing an arbitrary object placed inside the cloak.

and radius $a = 0.7\lambda$. The incident plane wave, as depicted in Figure 23, has a z-polarized E-field and traveled in the x-direction (left to right in Figures 23 and 24A–B). Whereas a shadow region existed when the cloak is switched off, the plane wave flowed through the object unhindered when the cloak was activated. More recently, it was shown that the cloak does not need to conform to the shape of the object being concealed. Figure 24C shows an example simulation where a square-shaped cloak concealed an arbitrarily shaped object within the region enclosed by the cloak. Essentially, the active HMS generates a zero field region interior to the cloak, such that objects within would not generate electromagnetic scattering and were thus concealed from the region exterior to the cloak. While the examples shown here demonstrate active electromagnetic cloaking in 2D, the principle would extend directly into three-dimensional with the involvement of properly directed electric and magnetic currents that form the solution to (10).

Active electromagnetic cloaking has been demonstrated experimentally using an HMS [28]. Figure 25A shows the parallel-plate waveguide environment in which the experiment was performed. A metallic cylinder of radius $a = 0.56\lambda$ ($f = 1$ GHz) was cloaked by an active HMS. The metallic shell of the cylinder shorted out the electric currents; the magnetic currents, calculable by (10), were implemented by small loops in close proximity to the cylinder. The cylinder was placed in a parallel-plate waveguide environment, with a perforated top plate, which allowed the probe to scan the electric field within the waveguide. A monopole source illuminated the environment from 3λ away. The measured total electric field (real-part) showed the existence of a shadow region when the cloak was removed (Figure 25B) and the restoration of the incident wave when the cloak was activated (Figure 25C). This work inspired the proposal of other active cloaking schemes, which included a parity-time symmetric cloak with both active and loss components [148].

While the active Huygens' cloak engineers the electromagnetic field external to the metasurface, a related development, which we call the Huygens' box, investigated the possibilities for engineering an electromagnetic waveform within a region enclosed by an HMS. Again invoking the equivalence principle, one can synthesize electric and magnetic currents along a closed surface, which result to the generation of an arbitrary waveform
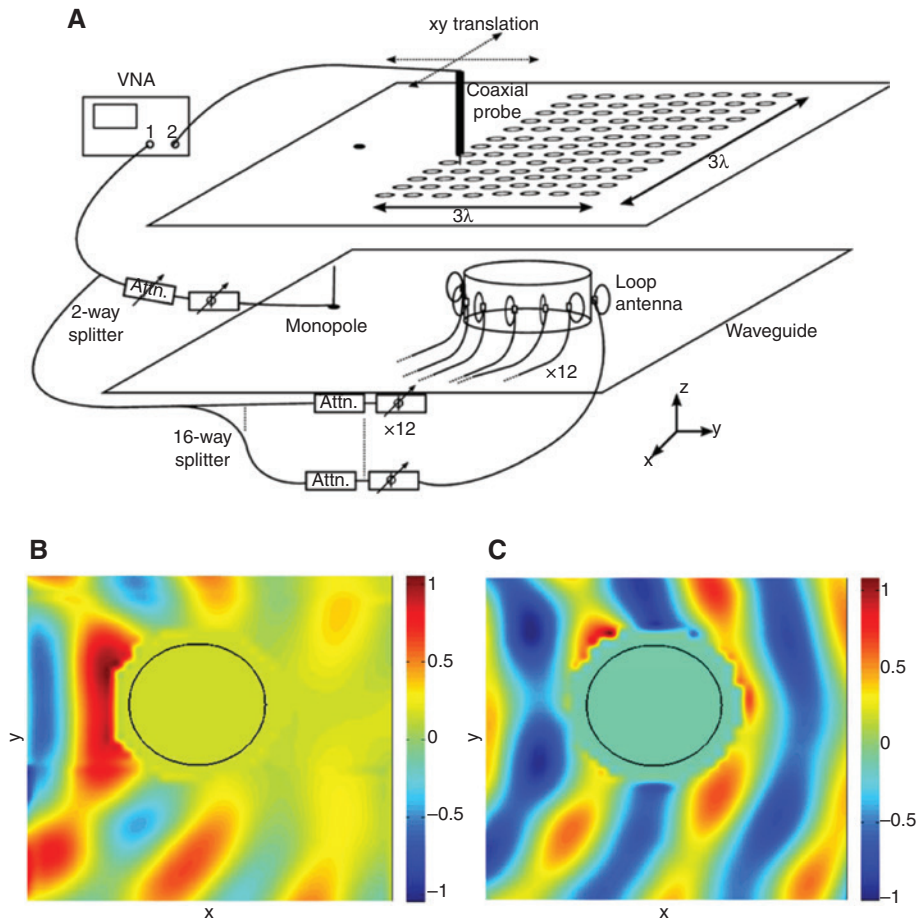
Figure 25: Experimental demonstration for active cloaking at $f=1$ GHz with an HMS.
(A) A schematic of the measurement setup. Obtained from [28]. (B) The measured total electric field (real part) with the cloak disabled. Obtained from [28]. (C) The measured total field (real part) with the cloak enabled. For practical reasons, the field strength inside the cloak is left unmeasured and rendered as zero-field in (B) and (C). Obtained from [28].

inside the enclosed region. We synthesized the required currents using a simple active Huygens' source element [149, 150], comprising a current strip or a dipole in close proximity to a metallic cavity wall, which shorted out the electric current and left only the magnetic dipole response through the image current. Using this device, we designed metasurfaces that generated unconventional modes within a metallic cavity. Figure 26 shows fullwave simulations performed at 1 GHz for a square metallic cavity of size $\lambda \times \lambda$. (The third (z-) dimension is made smaller than half-wavelength to render the cavity a 2D environment.) Travelling waves of arbitrary amplitude, phase, and propagation direction can be generated (Figure 26A–B); standing waves can also be generated with strong tangential electric fields very close to the metallic cavity walls (Figure 26C) [150]. The generation of these modes, which are naturally forbidden in a metallic cavity environment, allows one to build an arbitrary waveform by way of Fourier plane-wave superposition. Accordingly, Figure

26D shows a subwavelength focus formed by propagating plane waves, using a theory known as selective superoscillation [151]. Such waveforms can find potential use in medical imaging and hyperthermia – localized heating of the human body as part of a medical treatment procedure [152]. An ongoing effort towards experimental demonstration of arbitrary waveform generation in a Huygens' box has also been described in Ref. [150].

4 Conclusion and prospects

From the exposition of the basic principles and the various applications of HMSs described in this review paper, the versatility and effectiveness of HMSs in manipulating electromagnetic waves become apparent. Compared to gratings, including holographic ones, HMSs offer complete control over the excited Floquet modes, allowing the
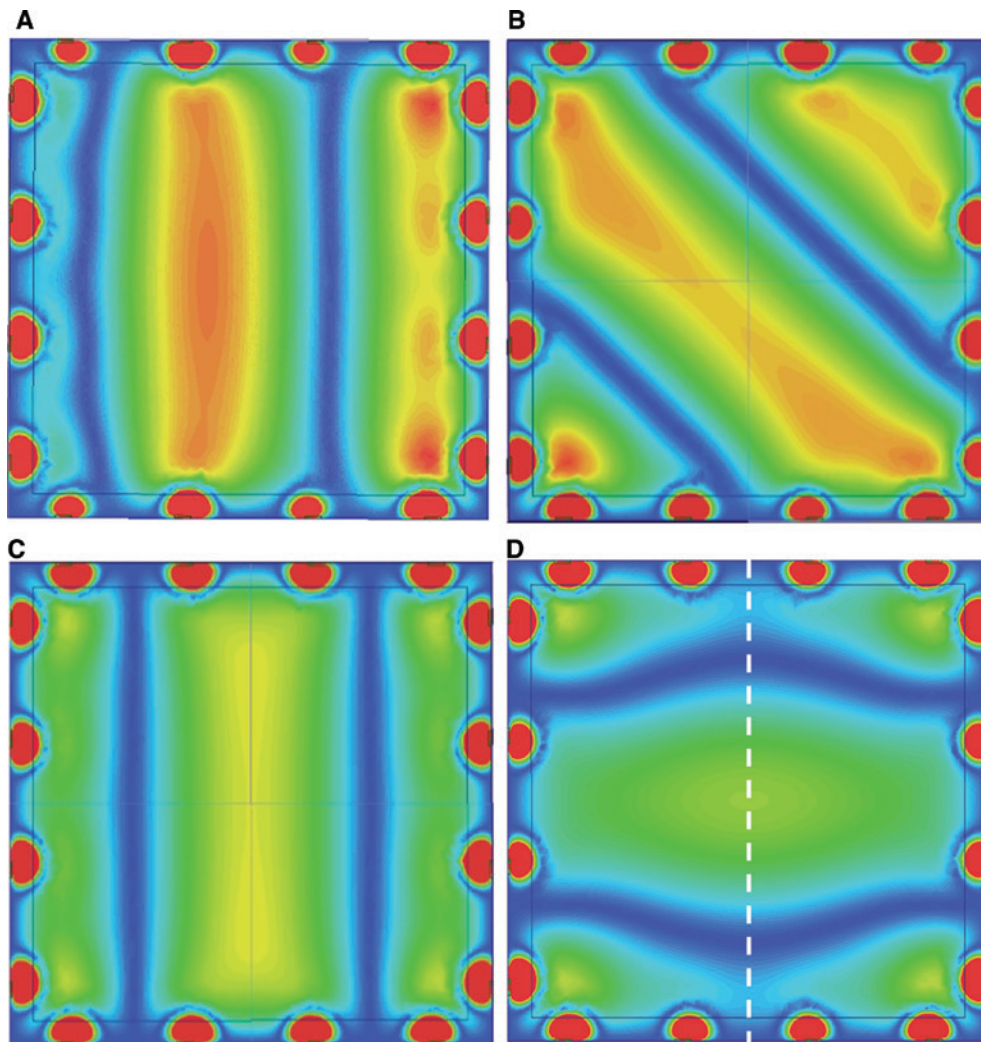
Figure 26: Fullwave simulation results for arbitrary wavefront generation using an active HMS.
(A) A travelling wave in the horizontal direction (obtained from [150]); (B) a travelling wave in the diagonal direction, 45° from the horizontal (*x*-) axis (obtained from [150]); (C) a standing wave in the *x*-direction, with electric field maxima very close to the metallic side walls (obtained from [150]); and (D) a superoscillation wave with a subwavelength focus at the image plane *y* = 0 (denoted by the white dashed line). Obtained from [150]. For subfigures (A) and (B), the real part of the electric field phasor is plotted; for subfigures (C) and (D), the electric field phasor amplitude is plotted.

suppression of unwanted spurious radiation. In addition, compared to reflect- and transmitarrays, they can be made subwavelength thin while offering perfect conversion efficiency between the incident and reflected/refracted waves. The HMSs can be realized from microwaves to optics using both metallic and purely dielectric structures.

Prospects for the future look bright. The possibility of inducing auxiliary surface waves in the design of HMSs offers a way for even more complex wave manipulations such as beam splitting and novel antenna functionality [63]. In the optical regime, nanoscale thin lenses can be envisioned to further miniaturize personal communication devices [18]. Equipping the HMSs unit cells with various control elements such as varactors at microwaves and liquid crystals or phase-transition materials in the optical regime can open up new possibilities for antenna and optical beam-forming applications. One can also envision loading the unit cells with non-linear or non-reciprocal elements to synthesize new functionalities such as frequency conversion, optical switching, and wave isolation/duplexing [153, 154]. Time modulating HMS is another possibility for obtaining various parametric effects, including magnetless non-reciprocity [155]. Finally, the front of active HMSs, as described in Section 3.5, offers many possibilities for future developments such as active cloaking, steerable antennas, and beam focusing for medical applications.

References

[1] Rudge AW, Adatia NA. Offset-parabolic-reflector antennas: a review. Proc IEEE 1978;66:1592–618.

[2] Jones E. Paraboloid reflector and hyperboloid lens antennas. Trans IRE Prof Group Antennas Propag 1954;2:119–27.

[3] Wu X, Eleftheriades GV, van Deventer-Perkins TE. Design and characterization of single- and multiple-beam mm-wave circularly polarized substrate lens antennas for wireless communications. IEEE Trans Microw Theory Tech 2001;49:431–41.

[4] Born M, Wolf E. Principle of optics, 6th ed. New York: Pergamon Press, 1980.

[5] Huang J, Encinar JA. Reflectarray antennas. Hoboken, NJ, USA: Wiley, 2007.

[6] Pozar DM. Flat lens antenna concept using aperture coupled microstrip patches. Electron Lett 1996;32:2109–11.

[7] Ryan CGM, Chaharmir MR, Shaker JRBJ, Antar YMM, Ittipiboon A. A wideband transmit-array using dual-resonant double square rings. IEEE Trans Antennas Propag 2010;58:1486–93.

[8] Li M, Behdad N. Wideband true-time-delay microwave lenses based on metallo-dielectric and all-dielectric lowpass frequency selective surfaces. IEEE Trans Antennas Propag 2013;61:4109–19.

[9] Hum SV, Perruisseau-Carrier J. Reconfigurable reflectarrays and array lenses for dynamic antenna beam control: a review. IEEE Trans Antennas Propag 2014;62:183–98.

[10] Goodman J. Introduction to Fourier optics, 3rd ed. Englewood, CO, USA: Roberts and Company, 2004.

[11] Gaylord T, Moharam M. Analysis and applications of optical diffraction by gratings. Proc IEEE 1985;73:894–937.

[12] Lukosz W. Optical systems with resolving powers exceeding the classical limit I. J Opt Soc Am 1966;56:1463–72.

[13] Iizuka K, Mizusawa M, Urasaki S, Ushigome H. Volume-type holographic antenna. IEEE Trans Antennas Propag 1975;23:807–10.

[14] Gallagher NC, Sweeney DW. Computer-generated microwave kinoforms. Opt Eng 1989;28:599–604.

[15] Weiner AM. Femtosecond pulse shaping and processing. Prog Quantum Electron 1995;19:161–237.

[16] Ebbesen TW, Lezec HJ, Ghaemi HF, Thio T, Wolff PA. Extraordinary optical transmission through sub-wavelength hole arrays. Nature 1998;391:667–9.

[17] Yu N, Genevet P, Kats Ma, Aieta F, Tetienne J-P, Capasso F, Gaburro Z. Light propagation with phase discontinuities: generalized laws of reflection and refraction. Science 2011;334:333–7.

[18] Yu N, Capasso F. Flat optics with designer metasurfaces. Nat Mater 2014;13:139–50.

[19] Fong BH, Colburn JS, Ottusch JJ, Visher JL, Sievenpiper DF. Scalar and tensor holographic artificial impedance surfaces. IEEE Trans Antennas Propag 2010;58:3212–21.

[20] Minatti G, Caminita F, Martini E, Sabbadini M, Maci S. Synthesis of modulated-metasurface antennas with amplitude, phase and polarization control. IEEE Trans Antennas Propag 2013;64:3907–19.

[21] Pfeiffer C, Grbic A. Metamaterial Huygens' surfaces: tailoring wave fronts with reflectionless sheets. Phys Rev Lett 2013;110:197401.

[22] Selvanayagam M, Eleftheriades GV. Discontinuous electromagnetic fields using orthogonal electric and magnetic currents for wavefront manipulation. Opt Express 2013;3727:3720–7.

[23] Monticone F, Estakhri NM, Alù A. Full control of nanoscale optical transmission with a composite metascreen. Phys Rev Lett 2013;110:203903.

[24] Holloway CL, Kuester EF, Gordon JA, O'Hara J, Booth J, Smith DR. An overview of the theory and applications of metasurfaces: the two-dimensional equivalents of metamaterials. IEEE Antennas Propag Mag 2012;54:10–35.

[25] Harrington R. Time-harmonic electromagnetic fields. New York, USA: Wiley, 2001, ch. 3.

[26] Wong JPS, Selvanayagam M, Eleftheriades GV. Design of unit cells and demonstration of methods for synthesizing Huygens' metasurfaces. Photonics Nanostructures – Fundam Appl 2014;12:360–75.

[27] Selvanayagam M, Eleftheriades GV. An active electromagnetic cloak using the equivalence principle. IEEE Antennas Wireless Propagat Lett 2012;11;1226–9.

[28] Selvanayagam M, Eleftheriades GV. Experimental demonstration of active electromagnetic cloaking. Phys Rev X 2013;3:041011.

[29] Epstein A, Eleftheriades GV. Floquet-Bloch analysis of refracting Huygens' metasurfaces. Phys Rev B 2014;90:235127.

[30] Asadchy V, Faniayeu I, Ra'di Y, Khakhomov S, Semchenko I, Tretyakov S. Broadband reflectionless metasheets: frequency-selective transmission and perfect absorption. Phys Rev X 2015;5:031005.

[31] Landy NI, Sajuyigbe S, Mock JJ, Smith DR, Padilla WJ. Perfect metamaterial absorber. Phys Rev Lett 2008;100:207402.

[32] Liu N, Mesch M, Weiss T, Hentschel M, Giessen H. Infrared perfect absorber and its application as plasmonic sensor. Nano Lett 2010;10:2342–8.

[33] Diem M, Koschny T, Soukoulis CM. Wide-angle perfect absorber/thermal emitter in the terahertz regime. Phys Rev B 2009;79;033101.

[34] Schelkunoff SA. Some equivalence theorems of electromagnetics and their application to radiation problems. Bell Syst Tech J 1936;15;92–112.

[35] Balanis C. Advanced engineering electromagnetics. New York, USA: Wiley, 2012.

[36] Kuester E, Mohamed M, Piket-May M, Holloway C. Averaged transition conditions for electromagnetic fields at a metafilm. IEEE Trans Antennas Propag 2003;51:2641–51.

[37] Achouri K, Salem M, Caloz C. General metasurface synthesis based on susceptibility tensors. IEEE Trans Antennas Propag 2015;63;2977–91.

[38] Albooyeh M, Tretyakov S, Simovski C. Electromagnetic characterization of bianisotropic metasurfaces on refractive substrates: general theoretical framework. Ann Phys (Berl) 2016;528:721–7.

[39] Holloway CL, Mohamed MA, Kuester EF, Dienstfrey A. Reflection and transmission properties of a metafilm: with an application to a controllable surface composed of resonant particles. IEEE Trans Electromag Compat 2005;47:853–65.

[40] Niemi T, Karilainen AO, Tretyakov S. Synthesis of polarization transformers. IEEE Trans Antennas Propag 2013;61:3102–11.

[41] Epstein A, Eleftheriades GV. Huygens' metasurfaces via the equivalence principle: design and applications. J Opt Soc Am B 2016;33;A31–50.

[42] Epstein A, Eleftheriades GV. Arbitrary power conserving field transformations with passive lossless omega-type

bianisotropic metasurfaces. IEEE Trans Antennas Propag 2016;64:3880–95.

[43] Selvanayagam M, Eleftheriades GV. Polarization control using tensor Huygens' surfaces. IEEE Trans Antennas Propag 2014;62:6155–68.

[44] Pfeiffer C, Zhang VRC, Guo J, Grbic A. Polarization rotation with ultra-thin bianisotropic metasurfaces. Optica 2016;3:427–32.

[45] Epstein A, Eleftheriades GV. Passive lossless Huygens' metasurfaces for conversion of arbitrary source field to directive radiation. IEEE Trans Antennas Propag 2014;62:5680–95.

[46] Tretyakov SA. Metasurfaces for general transformations of electromagnetic fields. Phil Trans R Soc A Mathematical Phys Eng Sci 2015;373:20140362.

[47] Huygens C. Traité de la Lumière. Leiden: Pierre vander Aa, 1690.

[48] Ra'di Y, Asadchy VS, Tretyakov SA. One-way transparent sheets. Phys Rev B 2014;89:075109.

[49] Kim M, Wong AMH, Eleftheriades GV. Optical Huygens' metasurfaces with independent control of the magnitude and phase of the local reflection coefficients. Phys Rev X 2014;4:041042.

[50] Wong JPS, Selvanayagam M, Eleftheriades GV. Polarization considerations for scalar Huygens' metasurfaces and characterization for 2-D refraction. IEEE Trans Microw Theory Techn 2015;63:913–24.

[51] Pfeiffer C, Emani NK, Shaltout AM, Boltasseva A, Shalaev VM, Grbic A. Efficient light bending with isotropic metamaterial Huygens' surfaces. Nano Lett 2014;14:2491–7.

[52] Pfeiffer C, Grbic A. Bianisotropic metasurfaces for optimal polarization control: analysis and synthesis Phys Rev Appl 2014;2:044011.

[53] Epstein A, Wong JPS, Eleftheriades GV. Cavity-excited Huygens' metasurface antennas for near-unity aperture efficiency from arbitrarily large apertures. Nat Commun 2016;7:10360.

[54] Wong JPS, Epstein A, Eleftheriades GV. Reflectionless wide-angle refracting metasurfaces. IEEE Antennas Wireless Propag Lett 2015;15:1293–6.

[55] Asadchy VS, Albooyeh M, Tcvetkova SN, Daz-Rubio A, Ra'di Y, Tretyakov SA. Perfect control of reflection and refraction using spatially dispersive metasurfaces. Phys Rev B 2016;94:075142.

[56] Asadchy V, Albooyeh M, Tcvetkova S, Ra'di Y, Tretyakov SA. Metasurfaces for perfect and full control of refraction and reflection, in Proceedings of the 10th International Congress on Advanced Electromagnetic Materials in Microwaves and Optics (METAMATERIALS), Chania, Greece, 2016.

[57] Estakhri NM, Alù A. Recent progress in gradient metasurfaces. J Opt Soc Am B 2016;33:A21–30.

[58] Estakhri NM, Alù A. Wave-front transformation with gradient metasurfaces. Phys Rev X 2016;6:041008.

[59] Kong JA. Theorems of bianisotropic media. Proc IEEE 1972;60:1036–46.

[60] Chen M, Abdo-Sanchez E, Epstein A, Eleftheriades GV. Experimental verification of reflectionless wide-angle refraction via a bianisotropic Huygens' metasurface, in Proceedings of the XXXIInd URSI General Assembly and Scientific Symposium (URSI GASS), Montreal, Canada, 2017.

[61] Ra'di Y, Tretyakov SA. Balanced and optimal bianisotropic particles: maximizing power extracted from electromagnetic fields. New J Phys 2013;15:053008.

[62] Asadchy VS, Ra'di Y, Vehmas J, Tretyakov SA. Functional metamirrors using bianisotropic elements. Phys Rev Lett 2015;114:095503.

[63] Epstein A, Eleftheriades GV. Synthesis of passive lossless metasurfaces using auxiliary fields for reflectionless beam splitting and perfect reflection. Phys Rev Lett 2016;117:256103.

[64] Epstein A, Eleftheriades GV. Arbitrary antenna arrays without feed networks based on cavity-excited omega-bianisotropic metasurfaces. IEEE Trans Antennas Propag 2017;65:1749–56.

[65] Epstein A, Eleftheriades GV. Emulating arbitrary antenna arrays with low-profile probe-fed cavity-excited omega-bianisotropic metasurface antennas, in Proceedings of the 11th European Conference on Antennas and Propagation (EUCAP), Paris, France, 2017.

[66] Selvanayagam M, Eleftheriades GV. Circuit modelling of Huygens' surfaces. IEEE Antennas Wireless Propagat Lett 2013;12:1642–5.

[67] Dorrah A, Eleftheriades GV. All-pass characteristics of a Huygens' unit cell, in Proceedings of the 2018 United States Nat. Committee Radio Science Meeting (USNC-URSI NRSM), Boulder, CO, USA, 2018.

[68] Pozar D. Microwave engineering. Hoboken, NJ, USA: Wiley, 2012.

[69] Frickey DA. Conversions between S, Z, Y, h, ABCD, and T parameters which are valid for complex source and load impedances. IEEE Trans Microw Theory Techn 1994;42:205–11.

[70] Lavigne G, Achouri K, Asadchy V, Tretyakov S, Caloz C. Susceptibility derivation and experimental demonstration of refracting metasurfaces without spurious diffraction. IEEE Trans Antennas Propag 2018;66:1321–30.

[71] Wong AMH, Eleftheriades GV. Perfect anomalous reflection with a bipartite Huygens' metasurface. Phys Rev X 2018;8:011036.

[72] Asadchy VS, Wickberg A, Díaz-Rubio A, Wegener M. Eliminating scattering loss in anomalously reflecting optical metasurfaces. ACS Photonics 2017;4:1264–70.

[73] Díaz-Rubio A, Asadchy V, Elsakka A, Tretyakov SA. From the generalized reflection law to the realization of perfect anomalous reflectors. Sci Adv 2017;3:e1602714.

[74] Díaz-Rubio A, Tretyakov SA. Power-flow conformal metamirrors for engineering wave reflections. *arXiv:1710.06336* 2017.

[75] Jull EV, Beaulieu NC. An unusual reflection grating behaviour suitable for efficient frequency scanning, in Proceedings of the IEEE AP-S Int. Sym. Dig., Quebec, Canada, 1980.

[76] Cho YK, Ra JW, Cho UH, Lee JI. Off-bragg TE blazing of a periodic strip grating on a grounded dielectric. IET Electron Lett 1997;33:1446–7.

[77] Chen W, Beaulieu NC, Michelson DG, Jull EV. Off-bragg blazed rectangular groove gratings for high diffraction efficiency devices. IEEE Trans Antennas Propag 2013;61:2342–7.

[78] Maystre D, Cadilhac M. A phenomenological theory for gratings: perfect blazing for polarized light in nonzero deviation mounting. Radio Sci 1981;16:1003–8.

[79] Ra'di Y, Sounas DL, Alù A. Metagratings: beyond the limits of graded metasurfaces for wave front control. Phys Rev Lett 2017;119:067404.

[80] Epstein A, Rabinovich O. Unveiling the properties of metagratings via a detailed analytical model for synthesis and analysis. Phys Rev Appl 2017;8:054037.

[81] Wong AMH, Christian P, Eleftheriades GV. Binary Huygens' metasurface: a simple, efficient retroreflector at near-grazing

angles, in Proceedings of the 2017 United States Nat. Committee Radio Science Meeting (USNC-URSI NRSM), Boulder, CO, USA, 2017.

[82] Wong AMH, Christian P, Eleftheriades GV. Binary Huygens' metasurfaces: experimental demonstration of simple, efficient near-grazing retroreflectors for TE and TM polarizations. IEEE Trans Antennas Propag 2018, in press.

[83] Hessel A, Schmoys J, Tseng DY. Bragg-angle blazing of diffraction gratings. J Opt Soc Am 1975;65:380–4.

[84] Wong AMH, Eleftheriades GV. Perfect anomalous reflection with an aggressively discretized Huygens' metasurface, in Proceedings of the XXXIInd URSI General Assembly and Scientific Symposium (URSI GASS), Montreal, Canada, 2017.

[85] Pfeiffer C, Grbic A. Millimeter-wave transmitarrays for wavefront and polarization control. IEEE Trans Microw Theory Techn 2013;61:4407–17.

[86] Kim M, Jeong J, Poon JKS, Eleftheriades GV. Vanadium-dioxide-assisted digital optical metasurfaces for dynamic wavefront engineering. J Opt Soc Am B 2016;33:980–8.

[87] Huang Y-W, Lee HWH, Sokhoyan R, et al. Gate-tunable conducting oxide metasurfaces. Nano Lett 2016;16:5319–25.

[88] Pors A, Bozhevolnyi SI. Plasmonic metasurfaces for efficient phase control in reflection. Opt Express 2013;21:27438–51.

[89] Pors A, Albrektsen O, Radko IP, Bozhevolnyi SI. Gap plasmon-based metasurfaces for total control of reflected light. Sci Rep 2013;3:2155.

[90] Sun S, Yang K-Y, Wang C-M, et al. High-efficiency broadband anomalous reflection by gradient meta-surfaces. Nano Lett 2012;12:6223–9.

[91] Zheng G, Mühlenbernd H, Kenney M, Li G, Zentgraf T, Zhang S. Metasurface holograms reaching 80% efficiency. Nat Nanotechnol 2015;10:308–12.

[92] Mie G. "Beiträge zur optik trüber medien, speziell kolloidaler metallösungen. Ann Phys 1908;330:377–445.

[93] Lewin L. The electrical constants of a material loaded with spherical particles. Electrical Engineers – Part III: radio and communication engineering. J Inst 1947;94:65–8.

[94] Kerker M, Wang D-S, Giles CL. Electromagnetic scattering by magnetic spheres. J Opt Soc Am 1983;73:765–7.

[95] Wang Z, An N, Shen F, et al. Enhanced forward scattering of ellipsoidal dielectric nanoparticles. Nanoscale Res Lett 2017;12:58.

[96] García-Cámara B, de la Osa RA, Saiz JM, González F, Moreno F. Directionality in scattering by nanoparticles: Kerker's null-scattering conditions revisited. Opt Lett 2011;36:728–30.

[97] Vynck K, Felbacq D, Centeno E, Căbuz AI, Cassagne D, Guizal B. All-dielectric rod-type metamaterials at optical frequencies. Phys Rev Lett 2009;102:133901.

[98] Evlyukhin AB, Reinhardt C, Chichkov BN. Multipole light scattering by nonspherical nanoparticles in the discrete dipole approximation. Phys Rev B 2011;84:235429.

[99] Kuznetsov AI, Miroshnichenko AE, Fu YH, Zhang J, Luk'yanchuk B. Magnetic light. Sci Rep 2012;2:492.

[100] Fu YH, Kuznetsov AI, Miroshnichenko AE, Yu YF, Luk'yanchuk B. Directional visible light scattering by silicon nanoparticles. Nat Commun 2013;4:1527.

[101] Person S, Jain M, Lapin Z, Sáenz JJ, Wicks G, Novotny L. Demonstration of zero optical backscattering from single nanoparticles. Nano Lett 2013;13:1806–9.

[102] Cheng J, Ansari-Oghol-Beig D, Mosallaei H. Wave manipulation with designer dielectric metasurfaces. Opt Lett 2014;39:6285–8.

[103] Decker M, Staude I, Falkner M, et al. High-efficiency dielectric Huygens' surfaces. Adv Opt Mater 2015;3:813–20.

[104] Staude I, Miroshnichenko AE, Decker M, et al. Tailoring directional scattering through magnetic and electric resonances in subwavelength silicon nanodisks. ACS Nano 2013;7:7824–32.

[105] Özdemir A, Hayran Z, Takashima Y, Kurt H. Polarization independent high transmission large numerical aperture laser beam focusing and deflection by dielectric Huygens' metasurfaces. Opt Commun 2017;401:46–53.

[106] Shanei MM, Hashemi M, Fathi D, Zapata-Rodríguez CJ. Dielectric metalenses with engineered point spread function. Appl Opt 2017;56:8917–23.

[107] Guo Z, Tian L, Shen F, Zhou H, Guo K. Mid-infrared polarization devices based on the double-phase modulating dielectric metasurface. J Phys D Appl Phys 2017;50:254001.

[108] Iyer PP, Pendharkar M, Schuller JA. Electrically reconfigurable metasurfaces using heterojunction resonators. Adv Opt Mat 2016;4:1582–8.

[109] Liu S, Vaskin A, Campione S, et al. Huygens' metasurfaces enabled by magnetic dipole resonance tuning in split dielectric nanoresonators. Nano Lett 2017;17:4297–303.

[110] Forouzmand A, Mosallaei H. All-dielectric C-shaped nanoantennas for light manipulation: Tailoring both magnetic and electric resonances to the desire. Adv Opt Mater 2017;5:700:147.

[111] Tian J, Yang Y, Qiu M, Laurell F, Pasiskevicius V, Jang H. All-dielectric KTiOPO4 metasurfaces based on multipolar resonances in the terahertz region. Opt Express 2017;25:24068–80.

[112] Arslan D, Chong KE, Miroshnichenko AE, et al. Angle-selective all-dielectric Huygens' metasurfaces. J Phys D Appl Phys 2017;50:434002.

[113] Khaidarov E, Hao H, Paniagua-Dominguez R, et al. Asymmetric nanoantennas for ultrahigh angle broadband visible light bending. Nano Lett 2017;17:6267–72.

[114] Zhao W, Jiang H, Liu B, et al. Dielectric Huygens' metasurface for high-efficiency hologram operating in transmission mode. Sci Rep 2016;6:30613.

[115] Komar A, Fang Z, Bohn J, et al. Electrically tunable all-dielectric optical metasurfaces based on liquid crystals. Appl Phys Lett 2017;110:071109.

[116] Paniagua-Dominguez R, Yu YF, Miroshnichenko AE, et al. Generalized Brewster effect in dielectric metasurfaces. Nat Commun 2016;7:10362.

[117] Zuo H, Choi D-Y, Gai X, et al. High-efficiency all-dielectric metalenses for mid-infrared imaging. Adv Opt Mater 2017;5:1700585.

[118] Yu YF, Zhu AY, Paniagua-Dominguez R, Fu YH, Luk'yanchuk B, Kuznetsov AI. High-transmission dielectric metasurface with 2π phase control at visible wavelengths. Laser Photonics Rev 2015;9:412–8.

[119] Bar-David J, Mazurski N, Levy U. In situ planarization of huygens metasurfaces by nanoscale local oxidation of silicon. ACS Photonics 2017;4:2359–66.

[120] Dezert R, Richetti P, Baron A. Isotropic Huygens dipoles and multipoles with colloidal particles. Phys Rev B 2017;96:180201.

[121] Li Q-T, Dong F, Wang B, et al. Polarization-independent and high-efficiency dielectric metasurfaces for visible light. Opt Express 2016;24;16309–19.

[122] Chong KE, Staude I, James A, et al. Polarization-independent silicon metadevices for efficient optical wavefront control. Nano Lett 2015;15:5369–74.

[123] Yoon G, Lee D, Nam KT, Rho J. Pragmatic metasurface hologram at visible wavelength: the balance between diffraction efficiency and fabrication compatibility. ACS Photonics 2017. Doi: 10.1021/acsphotonics.7b01044.

[124] Iyer PP, Butakov NA, Schuller JA. Reconfigurable semiconductor phased-array metasurfaces. ACS Photonics 2015;2:1077–84.

[125] Babicheva VE, Petrov MI, Baryshnikova KV, Belov PA. Reflection compensation mediated by electric and magnetic resonances of all-dielectric metasurfaces (invited). J Opt Soc Am B 2017;34:D18–28.

[126] Babicheva VE, Evlyukhin AB. Resonant lattice Kerker effect in metasurfaces with electric and magnetic optical responses. Laser Photonics Rev 2017;11:1700132.

[127] Jia D, Tian Y, Ma W, et al. Transmissive terahertz metalens with full phase control based on a dielectric metasurface. Opt Lett 2017;42:4494–7.

[128] Shcherbakov MR, Liu S, Zubyuk VV, et al. Ultrafast all-optical tuning of direct-gap semiconductor metasurfaces. Nat Commun 2017;8:17.

[129] Kruk S, Hopkins B, Kravchenko II, Miroshnichenko A, Neshev DN, Kivshar YS. Invited article: broadband highly efficient dielectric metadevices for polarization control. APL Photonics 2016;1:030801.

[130] Sautter J, Staude I, Decker M, et al. Active tuning of all-dielectric metasurfaces ACS Nano 2015;9:4308–15.

[131] Polischuk OV, Melnikova VS, Popov VV. Giant cross-polarization conversion of terahertz radiation by plasmons in an active graphene metasurface. Appl Phys Lett 2016;109:131101.

[132] Popescu A, Ali T, Bendoym I, et al. Active metasurfaces, in Proceedings of Terahertz, RF, Millimeter and Submillimeter-Wave Tech. and Appl. VII, San Francisco, USA, 2014.

[133] Li Q, Tian Z, Zhang X, et al. Dual control of active graphene–silicon hybrid metamaterial devices. Carbon 2015;90:146–53.

[134] Chu CH, Tseng ML, Chen J, et al. Active dielectric metasurface based on phase-change medium. Laser Photon Rev 2016;10:986–94.

[135] Li T, Huang L, Liu J, Wang Y, Zentgraf T. Tunable wave plate based on active plasmonic metasurfaces. Opt Express 2017;24:4216–26.

[136] Su X, Ouyang C, Xu N, et al. Active metasurface terahertz deflector with phase discontinuities. Opt Express 2015;23:27152–8.

[137] Zhu BO, Zhao J, Feng Y. Active impedance metasurface with full 360° reflection phase tuning. Sci Rep 2013;3:3059.

[138] Yoo M, Lim S. Active metasurface for controlling reflection and absorption properties. Appl Phys Express 2014;7:112204.

[139] Chen K, Feng Y, Monticone F, et al. A reconfigurable active Huygens' metalens. Adv Mater 2017;29:1606422.

[140] Burokur SN, Daniel J, Ratajczak P, de Lustrac A. Low-profile frequency agile directive antenna based on an active metasurface. Micro Opt Technol Lett 2011;53:2291–5.

[141] Li W, Xia S, He B, et al. A reconfigurable polarization converter using active metasurface and its application in horn antenna. IEEE Trans Antennas Propag 2016;64:5281–90.

[142] Pendry JB, Schurig D, Smith DR. Controlling electromagnetic fields. Science 2016;312:1780–2.

[143] Alù A, Engheta N. Multifrequency optical invisibility cloak with layered plasmonic shells. Phys Rev Lett 2008;100:113901.

[144] Monticone F, Alù A. Do cloaked objects really scatter less? Phys Rev X 2013;3:041005.

[145] Miller DAB. On perfect cloaking. Opt Express 2006;14:12457–66.

[146] Vasquez FG, Milton GW, Onofrei D. Active exterior cloaking for the 2D Laplace and Helmholtz equations. Phys Rev Lett 2009;103:073901.

[147] Zheng HH, Xiao JJ, Lai Y, Chan CT. Exterior optical cloaking and illusions by using active sources: a boundary element perspective. Phys Rev B 2010;81:195116.

[148] Sounas DL, Fleury R, Alù A. Unidirectional cloaking based on metasurfaces with balanced loss and gain. Phys Rev Appl 2015;4:014005.

[149] Wong AMH, Eleftheriades GV. A simple active Huygens source for studying waveform synthesis with Huygens metasurfaces and antenna arrays, in Proceedings of the 2015 IEEE International Symposium on Antennas and Propagation & USNC/URSI National Radio Science Meeting (AP-S), Vancouver, BC, Canada, 2015.

[150] Wong AMH, Eleftheriades GV. Active Huygens' metasurfaces for RF waveform synthesis in a cavity, in Proceedings of the 18th Mediterranean Electrotechnical Conference (MELECON), Lemesos, Cyprus, 2016.

[151] Wong AMH, Eleftheriades GV. Superoscillations without sidebands: power efficient sub-diffraction imaging with propagating waves. Sci Rep 2015;5:8449.

[152] Ludwig A, Wong JPS, Epstein A, Wong AMH, Eleftheriades GV, Sarris CD. Focusing and steering for medical applications with magnetic near-field arrays and metasurfaces, in Proceedings of the 9th European Conference on Antennas and Propagation (EuCAP), Lisbon, Portugal, 2015.

[153] Li G, Zhang S, Zentgraf T. Nonlinear photonic metasurfaces. Nat Rev Mater 2017;2:17010.

[154] Chen S, Fan F, Wang X, Wu P, Zhang H, Chang S. Terahertz isolator based on nonreciprocal magneto-metasurface. Opt Express 2015;23:1015–24.

[155] Alù A. Enhancing metasurfaces and metamaterials with time-modulation and nonlinear responses, in Proceedings of the 10th International Congress on Advanced Electromagnetic Materials in Microwaves and Optics (METAMATERIALS), Chania, Greece, 2016.